

Journal Pre-proof

A Consistent Method for Direct Numerical Simulation of Droplet Evaporation

Jonathan Reutzsch, Corine Kieffer-Roth, Bernhard Weigand

PII: S0021-9991(20)30229-1
DOI: <https://doi.org/10.1016/j.jcp.2020.109455>
Reference: YJCPH 109455

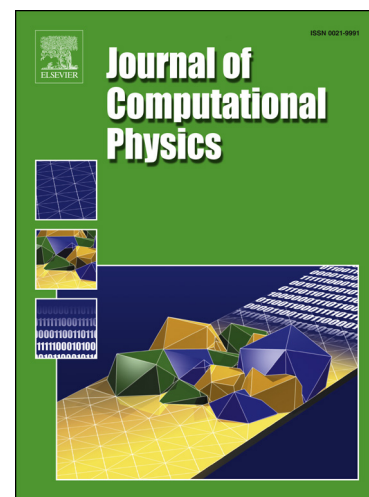
To appear in: *Journal of Computational Physics*

Received date: 9 January 2020
Revised date: 30 March 2020
Accepted date: 31 March 2020

Please cite this article as: J. Reutzsch et al., A Consistent Method for Direct Numerical Simulation of Droplet Evaporation, *J. Comput. Phys.* (2020), 109455, doi: <https://doi.org/10.1016/j.jcp.2020.109455>.

This is a PDF file of an article that has undergone enhancements after acceptance, such as the addition of a cover page and metadata, and formatting for readability, but it is not yet the definitive version of record. This version will undergo additional copyediting, typesetting and review before it is published in its final form, but we are providing this version to give early visibility of the article. Please note that, during the production process, errors may be discovered which could affect the content, and all legal disclaimers that apply to the journal pertain.

© 2020 Published by Elsevier.



Highlights

- Incompressible DNS based on Volume of Fluid method
- New method for evaporation of droplets
- Modelling of evaporation processes accounting for low and high evaporation rates
- Validation cases: Couette flow, droplets in an air flow, deformed droplets, levitated droplet
- Simulation results: evaporation of supercooled droplets, droplet oscillation and droplet with high evaporation rates

A Consistent Method for Direct Numerical Simulation of Droplet Evaporation

Jonathan Reutzsch*, Corine Kieffer-Roth, Bernhard Weigand

*Institut für Thermodynamik der Luft- und Raumfahrt (ITLR), Universität Stuttgart,
Pfaffenwaldring 31, 70569 Stuttgart, Germany*

Abstract

A consistent method for direct numerical simulations of evaporation processes is presented. It is implemented into the CFD code FS3D which solves the incompressible Navier-Stokes equations and is based on a Volume-of-Fluid method. In the new framework convection of the fluid and the gaseous phase is conducted first, whereas the physics of the phase change is captured subsequently in a fully consistent loop.

We present several validation cases and show, that the method is able to simulate evaporation processes for a large range of ambient conditions, ranging from supercooled droplets to extreme environments with high evaporation rates. Comparisons to analytical models from literature and other experimental investigations are in very good agreement.

Then, the method is applied for several three-dimensional direct numerical simulations of evaporating droplets. We present simulations of supercooled droplets in an airflow and compare them to experimental data. Furthermore, an oscillating droplet with evaporation is simulated and evaluated regarding the influence of the phase change on the droplet oscillation behavior. The potential of the method is also demonstrated for a free falling droplet in a high pressure and temperature atmosphere. Vapor fields and temperature regimes are evaluated in this case and show very good agreement to experiments.

Keywords: VOF, evaporation, droplets, multiphase flow, DNS, Stefan flow

1. Introduction

The phase change between a fluid and a gas is one of the most challenging issues in multiphase flows. Evaporation and condensation processes are governed by heat and mass transfer across the interface between the liquid and gaseous phases and are encountered in many scientific and technical applications. From

*Corresponding author

Email address: jonathan.reutzsch@itlr.uni-stuttgart.de (Jonathan Reutzsch)

Nomenclature

Symbols			Re	Reynolds number	—
A	surface area	m^2	ρ	density	kg m^{-3}
a, b, c	exponents for Wagner equation	—	\mathbf{S}	viscous stress tensor	N m^{-2}
a_z, a_r	axial and radial semi-axes	m	Sc	Schmidt number	—
α	relaxation factor	—	Sh	Sherwood number	m
A_{km}	oscillation modes	—	σ	surface tension	N m^{-1}
B_M	mass transfer number	—	S_{plic}	area of reconstructed interface	m^2
β	mass transfer coefficient	m s^{-1}	T	temperature	K
c_p	specific heat capacity	$\text{J kg}^{-1} \text{K}^{-1}$	t	time	s
D	diameter	m	\mathbf{u}	velocity vector, $\mathbf{u} = (u, v, w)^T$	m s^{-1}
\mathcal{D}_{bin}	binary diffusion coefficient	$\text{m}^2 \text{s}^{-1}$	V	interface velocity	m s^{-1}
δ	distance	m	V_Γ	growth velocity	m s^{-1}
ε	axes ratio	—	w	wetting	m
ε_Γ	threshold value	—	ω	oscillation frequency	m
F	flux per area	m s^{-1}	X	mass ratio	—
f	VOF-variable	—	x	vapor concentration	mol mol^{-1}
f_1	liquid volume fraction	—	Sub- and superscripts		
f_2	vapor volume fraction	—	$*$	dimensionless	
\mathbf{f}_γ	body force	$\text{m}^3 \text{s}^{-1}$	Γ	interface	
g	mass transfer conductance	$\text{kg m}^{-2} \text{s}^{-1}$	amb	ambient	
\mathbf{g}	volume forces	$\text{m}^2 \text{s}^{-1}$	c	continuous	
H_v	latent heat	J kg^{-1}	cr	critical	
k	heat conductivity	$\text{W m}^{-1} \text{K}^{-1}$	d	disperse	
\dot{m}''	area specific mass source	$\text{kg m}^{-2} \text{s}^{-1}$	g	gas	
κ	curvature	m^{-1}	gp	gaseous phase	
\dot{m}'''	volumetric mass source	$\text{kg m}^{-3} \text{s}^{-1}$	l	liquid	
L	deviation	m	m	iteration	
m	modes	—	n	normal vector component	
N	number of cells	—	osc	oscillation	
\mathbf{n}	normal vector	—	r	reduced	
n_{1-4}	material constants	—	rel	relative	
η_{vap}	dimensionless vapor flux	—	sat	saturation	
p	pressure	Pa	v	vapor	
\dot{q}'''	volumetric heat source	$\text{J m}^{-2} \text{s}^{-1}$	vol	volumetric	
R	Radius	m	x, y, z	directions	

6 weather phenomena, such as falling rain drops, fog and cloud formation in high
7 altitudes [49] to numerous industrial applications, like medical inhalation sprays,
8 spray combustion [14] and spray drying [43], phase change is present almost ev-
9 erywhere in our daily life. Therefore, the knowledge of these processes is an
10 important field of research and essential for the understanding of natural and
11 engineering systems.
12 Prevalently, when dealing with evaporation processes, focus is often put on the

phase change of droplets. In contrast to boiling, which refers to the changing of the phase from a liquid to gaseous state at the boiling point, evaporation takes place below the boiling point in the presence of an ambient gas. The inert gas is unsaturated with vapor, therefore, evaporation is driven by the vapor gradient. In the present paper, we will focus on this phase change process. Even though there are several experimental approaches to investigate droplet evaporation (Birouk and Gökalp [5]), the mechanisms of mass and energy transfer within the phases are not fully understood [8]. Due to the small scales and high velocities it is challenging to completely reveal these mechanisms with experiments. Thus, analytical and numerical investigations are indispensable to investigate the mentioned phenomena. Besides analytical modeling of evaporation processes, Direct Numerical Simulations (DNS) can provide further insights into phase change of droplets and is generally applied in various studies. A comparison and classification of droplet evaporation using models as well as DNS is given by Duret et al. [10].

Models for droplet evaporation can be found e.g. in the classical review papers of Faeth [14], Sirignano [74], Aggarwal and Pen [1], and Sazhin [67]. Extended approaches, which reproduce experiments at various pressure regimes or near critical conditions of the fluid, were introduced by several authors, such as Harstad and Bellan [24], Yang and Wong [97], or Lupo and Duwig [41]. Tonini and Cossali [85] developed an exact analytical solution for steady-state evaporation of a droplet in a stagnant environment and investigated the effect of oscillation on droplet evaporation. They extended the approach in [86, 87].

When looking at more complex structures and setups, such as strongly deformed droplets, droplets in a high velocity surrounding gas, evaporating droplet groups or sprays, evaporation models eventually lose their validity. In these cases, one requires a three-dimensional and transient numerical approach, thus, DNS is used to resolve the gas-liquid interface and solves the dynamics of the flow employing first principles. These are conservation of mass, momentum, and energy. DNS can be applied in a broader range of conditions, however, the physical modeling is challenging and it leads to high computational costs. Although many studies over the last decades have been conducted, 3D simulation of multiphase flow with evaporation is still one of the big challenges in CFD. The methods can be categorized in two main classes - on the one hand *interface tracking methods* and on the other hand *interface capturing methods*. Both attempt managing the difficulties of multiphase flow, such as the localization of the interface, variation of fluid properties, calculation of curvature and surface tension, vaporization conditions at the interface or the conservation of mass.

Tracking methods, like moving mesh, front tracking boundary integral, and particle schemes, are of Lagrangian type. They describe the interface directly as part of the computational mesh. Several papers about interface tracking can be found in literature, starting from the classical reviews of Hyman [33] and the group of Tryggvason [91, 89, 35] and Glimm [18, 19] to Popinet and Zaleski [48], Shyy et al. [73] and Tornberg [88]. One main advantage of the tracking methods is the accuracy of the interface shape calculation. This is particularly convenient for simulations with evaporation or condensation, where

physics strongly depends on the correct calculation of heat and mass fluxes at the interface. However, difficulties exist for simulations with strong deformations of the interface or droplet breakup and collision processes. The group of Renksizbulut [57, 56, 55] used a moving mesh to investigate heat and mass transfer of droplets in gas flow and droplet evaporation rates. Furthermore, Haywood et al. [29, 31, 30] applied a similar method in order to investigate transient droplet evaporation. They used a moving mesh and analyzed the deformation of the droplet considering the behavior of the surface dependent on internal circulation, heating and variable material properties. However, these studies were restricted to two-dimensional, axisymmetric problems and to small Re numbers as well as intermediate Re numbers of $Re \geq 100$. Tryggvason's group [91] used a front tracking method, which solves the external flow on a stationary, Cartesian grid and, in addition, a body-fitted grid to track the interface. Hence, they were able to calculate the surface tension force precisely and capture jumps in the viscosity and density field. They performed two- and three-dimensional simulations of bubble motions and later they extended their method in [35, 90].

In capturing methods, such as continuum advection, phase field method and level set, the interface is reconstructed using suitable field variables, mainly fluid fractions. A further classification can be made among these methods: On the one hand the continuous interface capturing, such as level-set or phase field methods, where the interface is identified as the zero level-set of an auxiliary function. On the other hand discontinuous interface capturing methods, such as Volume-of-Fluid (VOF) methods, where the interface is a discontinuity line of a characteristic function. Capturing methods are appropriate for simulations of phenomena with high surface deformation and topological changes, due to the circumstance, that they contain no assumption about the connectivity of the interface. Even though there are several disadvantages, like the high computational effort, the difficulty of the convective transport (especially for VOF-methods, where for example a complicated reconstruction of the surface is needed) or the violation of mass conservation (particularly for level-set methods), capturing methods are prevalent in simulations of multiphase flow with phase change. The group of Son and Dhir [79, 77, 80, 78] used a level-set approach for the 2D-simulation of film boiling processes and investigated the influence of wall superheating and extended their studies to simulate the growth of single bubbles during boiling and the coalescence behavior. Furthermore, they investigated droplet evaporation of micro droplets recently using the level-set method [75, 76, 3]. Nguyen et al. [45] developed an approach for the simulation of incompressible flame discontinuities, where they coupled a level-set formulation with a Ghost Fluid method [15]. Gibou and Fedkiw [17] applied the same concept for the investigation of Stefan flow caused by phase change. Tanguy et al. [84] extended the method and, in addition, they developed a model for the calculation of the velocity of the surface during evaporation. However, the simulations were limited to 2D and not validated with any experimental data or correlations. Despite several approaches to cope with the problem of level-set being not mass-conservative [12, 83], most of the relevant DNS investigations

of multiphase flow with phase change were conducted using the VOF method. Welch and Wilson [95] introduced a VOF approach for flows with boiling processes in 2D. The method of Davidson and Rudmann [9] based on VOF employed the analogy between heat- and mass-transfer in order to calculate the transport processes of the interface. Their studies were restricted to axisymmetrical cases with low mass flow rates. Simulations of multicomponent droplets using the VOF method were presented by Banerjee [4]. Likewise, the results are limited to two-dimensional cases. Palmore and Desjardins [34] recently presented a VOF framework for interface-resolved simulations of vaporizing liquid-gas flows. They demonstrated one 3D simulation of an evaporating droplet at intermediate Reynolds number and showed that a correct prediction of the interface properties is necessary for simulations with vaporization.

Following the discussion above and regarding the requirements for DNS, the VOF-method seems to be a suitable choice to investigate phase change processes. Thus, the present study makes use of the inhouse code **Free Surface 3D** (FS3D [11]), which is based on the VOF-method. The work is a continuation of various authors from the group of Weigand, who have been dealing with phase change processes for many years using FS3D. Hase and Weigand [26, 27, 28, 25] were the first ones using FS3D to investigate heat transfer of deformed droplets and developed a simple evaporation model, based on empirical parameters. Thereafter, Schlottke and Weigand [71, 69] extended the method and performed simulations of evaporating 3D droplets in a flow at high Reynolds and Weber numbers. Later Schlottke et al. [70, 68] improved the heat and mass transfer using sharp temperature and concentration fields as well as variable material properties. Ma and Bothe [42] used FS3D and developed a two-scalar approach for heat transfer in order to model thermocapillary two-phase flows with evaporation. They put their emphasis on a clear distinction of the different velocities at the interface. Ruberto et al. [66, 65] performed simulations of evaporating supercooled liquid water droplets within a wide range of relative humidities and temperatures, which were in good agreement with their experiments. Reutzscher et al. [58] presented the first purely Eulerian DNS simulation of an evaporating jet during atomization and analyzed the influence of evaporation on the primary breakup. Several investigations on the phase change process from solid to liquid have been conducted by Rauschenberger et al. [51, 52] as well as Reitzle et al. [53]. The latter also extended the method to account for sublimation processes [54].

Considering the mentioned studies and the gained knowledge about simulations and modeling of phase change, this paper presents a new advanced and numerically very stable method for DNS with evaporation. Based on the described previous works with FS3D we now combine the advantages of the already implemented methods and improve the models. We developed and adapted new algorithms in order to optimize the code and the new modeling of evaporation with FS3D. All this is presented in Sec. 3. The mathematical background will be explained before in Sec. 2. Subsequently, we will show several validation cases in Sec. 4 and compare them to literature data, analytical models as well as previous models and calculations. Finally, various numerical results for evap-

151 oration processes of droplets are given in Sec. 5. We will show, that the phase
 152 change model is now capable of simulating evaporation processes for a large
 153 range of ambient conditions, ranging from supercooled droplets to near critical
 154 environments with high temperatures. Furthermore, we are able to make DNS
 155 calculations ranging from complex 3D interface structures or droplets in an ex-
 156 ternal flow at higher velocities to a nearly perfectly round droplet in a complete
 157 quiescent atmosphere without significant interface deforming due to parasitic
 158 currents or adverse velocity calculations.

159 2. Mathematical formulation in the one-field approach

160 In this section we will give an overview of the mathematical formalism, the
 161 conservation laws and jump conditions, as well as the modeling and numeri-
 162 cal implementation. The assumptions made in this work are specified in the
 163 following:

- 164 • only incompressible flow of a Newtonian fluid is considered
- 165 • the drop fluid is a pure substance
- 166 • viscous dissipation is neglected in both phases
- 167 • local thermodynamic equilibrium is assumed at the interface
- 168 • thermal radiation is not considered

169 2.1. Phase variables of the VOF-method

170 FS3D makes use of the VOF-method, which was developed by Hirt and
 171 Nichols [32]. As a consequence, we introduce field variables f_i . They represent
 172 the volume fraction of liquid ($i = 1$) and vapor ($i = 2$) in one cell. f_1 is defined
 173 as

$$f_1(x, t) = \begin{cases} 0 & \text{liquid phase (l)} \\]0; 1[& \text{at the interface} \\ 1 & \text{gaseous phase (gp)}. \end{cases} \quad (1)$$

174 Here f_2 corresponds to the volume fraction of vapor, where we assume an ideal
 175 mixture between vapor (v) and inert gas (g). Due to the VOF-method the
 176 material properties are calculated following the *one-field* formulation. Thus, for
 177 example the density ρ is composed of the partial densities and reads

$$\rho = \rho_l f_1 + \rho_v f_2 + (1 - f_1 - f_2) \rho_g. \quad (2)$$

178 Using the VOF variables and the local density of the gaseous phase

$$\rho_{gp} = \frac{\rho_v f_2 + (1 - f_1 - f_2) \rho_g}{1 - f_1}, \quad (3)$$

179 the vapor mass ratio X_v is defined by the ratio of the partial density (index p)
 180 to the density of the gaseous phase

$$X_v = \frac{\rho_{p,v}}{\rho_{gp}} = \frac{f_2}{1 - f_1} \frac{\rho_v}{\rho_{gp}}. \quad (4)$$

181 2.2. Conservation equations

182 The flow field is computed by solving the governing equations for mass, mo-
183 mentum and energy conservation. The differential form of the mass conservation
184 reads

$$\rho_t + \nabla \cdot (\rho \mathbf{u}) = 0, \quad (5)$$

185 where \mathbf{u} denotes the velocity vector. Applying the one-field formulation the
186 following transport equations of the VOF variables f_1 and f_2 can be derived:

$$(f_1)_t + \nabla \cdot (f_1 \mathbf{u}_l) = -\frac{\dot{m}'''}{\rho_l} \quad (6)$$

187

$$(f_2)_t + \nabla \cdot (f_2 \mathbf{u}_{gp}) = \nabla \cdot (\mathfrak{D}_{bin} \nabla f_2) + \frac{\dot{m}'''}{\rho_v}. \quad (7)$$

188 Here \dot{m}''' is the volumetric mass source of vapor and \mathfrak{D}_{bin} represents the binary
189 diffusion coefficient. Note, that we distinguish between the mean velocity of the
190 gaseous phase \mathbf{u}_{gp} and the liquid phase velocity \mathbf{u}_l .

191 The momentum conservation equation is given by

$$(\rho \mathbf{u})_t + \nabla \cdot [(\rho \mathbf{u}) \otimes \mathbf{u}] = \nabla \cdot (\mathbf{S} - \mathbf{I}p) + \rho \mathbf{g} + \mathbf{f}_\gamma, \quad (8)$$

192 where we have the static pressure p , the volume forces \mathbf{g} , such as gravity, and
193 the body force \mathbf{f}_γ , which is used to model surface tension in the vicinity of the
194 interface. The viscous stress tensor \mathbf{S} can be written as $\mathbf{S} = \mu [\nabla \mathbf{u} + (\nabla \mathbf{u})^T]$
195 for Newtonian fluids with μ representing the dynamic viscosity.

196 For the energy balance we use a two-field approach, introduced in [70]. For this,
197 we define two scalar temperature fields in the liquid T_l and in the gaseous phase
198 T_{gp} . Thus, we gain a more precise evolution of the temperature in the vicinity of
199 the interface and - in contrast to the one-field formulation - the jump condition
200 at the interface can be applied. The energy equation in temperature form for
201 both phases j - the gaseous (gp) and the liquid (l) - reads

$$(\rho_j c_{p,j} T_j)_t + \nabla \cdot (\rho_j c_{p,j} T_j \mathbf{u}_j) = \nabla \cdot (k_j \nabla T_j) + \dot{q}_j'''. \quad (9)$$

202 In this equation c_p denotes the specific heat capacity at constant pressure, k the
203 heat conductivity, and \dot{q}''' is a volumetric heat source.

204 2.3. Jump conditions, evaporation rate and growth velocity

205 We start with the mass balance, Eq. 5, and integrate over an infinitesimally
206 thin control volume containing the interface. Thus, one obtains the jump con-
207 dition

$$\rho_l (u_{l,n} - V_n) = \rho_{gp} (u_{gp,n} - V_n) \quad (10)$$

208 where index n denotes in general the component of a vector normal to the
209 interface and V is the velocity of the interface.

From the jump conditions one can derive the local area specific evaporation rate \dot{m}'' . The detailed derivation is shown in Appendix A. This results in

$$\dot{m}'' = \frac{1}{1 - X_v} \mathfrak{D}_{bin} \rho_{gp} \nabla X_v. \quad (11)$$

From the relation of the local area specific evaporation rate \dot{m}'' and the jump conditions (see Appendix A) one obtains

$$u_{l,n} - u_{gp,n} = \left(\frac{1}{\rho_{gp}} - \frac{1}{\rho_l} \right) \dot{m}'' . \quad (12)$$

Note, that this approach is slightly different from the approach used in previous works of e.g. Hase [27] and Schlottke [71]. We use the density of the gaseous phase instead of the vapor density. Our approach leads to a difference between gaseous and liquid velocity exactly at the interface. From this one can derive the divergence of the velocity, which will be discussed later. We consider different velocities of the vapor and gas phase due to the fact, that the vapor velocity has a convective part related to the mean velocity of the gaseous phase and, additionally, a diffusive part. For more details the reader is referred to Appendix B. Reitzle et al. [54] found the same result for the divergence of the velocity using a different approach.

Starting from the jump condition we now define the growth velocity $V_\Gamma = -\frac{\dot{m}''}{\rho_l}$, which is the velocity of the interface relative to the liquid phase solely caused by the phase change. We define it as positive for evaporation, and negative when considering condensation. We make the usual assumption, that the growth velocity is normal to the interface. Note, that V_Γ is different from the absolute velocity V_n , which describes the total velocity including the whole interface movement in the domain.

Following previous works (e.g. [70, 42]) the jump condition for the energy equation reads

$$\dot{q}_l + \dot{q}_{gp} = \dot{m}'' \Delta H_v. \quad (13)$$

with $\dot{q}_l = -k_l(\nabla T_l)_n$ (Fouriers law), $\dot{q}_{gp} = -k_{gp}(\nabla T_{gp})_n$ and ΔH_v denotes the latent heat of vaporization. Note, that the flux is positive when it enters the considered phase.

The saturation pressure for vapor p_{sat} is estimated using the Wagner-equation [94]

$$\ln p_r = \frac{1}{T_r} (n_1 \tau + n_2 \tau^a + n_3 \tau^b + n_4 \tau^c), \quad (14)$$

where the reduced pressure p_r is the ratio of the saturation pressure to the critical pressure $p_r = \frac{p_{sat}}{p_c}$ and the reduced temperature is the ratio of the local and critical temperature $T_r = \frac{T}{T_c}$, respectively. Furthermore, $\tau = 1 - T_r$ and n_1, n_2, n_3 , and n_4 are material specific constants, which can be taken from corresponding tables, e.g. [46, 16]. For simulations with water the exponents are $a = 1.5$, $b = 3.0$, and $c = 6.0$, for simulations with other substances such as alkanes they read $a = 1.5$, $b = 2.5$, and $c = 5.0$ [46]. Other approaches of

calculating the vapor pressure are implemented in FS3D, such as the classical Antoine-equation [2] or the estimation following Xiang [96]. For the simulations presented here the differences between these methods are marginal, however, for special cases the results could vary slightly.

3. Numerical approach

In this section, the numerical methods to improve the implementation of evaporation processes in the in-house code FS3D are presented. The program is a CFD code and solves the incompressible Navier-Stokes equations as well as the energy equation by applying DNS in a VOF framework. FS3D is written in Fortran90 and is fully parallelized using OpenMP and MPI. Due to the VOF method the reconstruction of the interface is achieved using the Piecewise Linear Interface Calculation (PLIC) method proposed by Rider and Kothe [60]. All variables are stored on a Marker and Cell (MAC) grid [23], hence, velocities are stored on cell faces, scalars at cell centers, respectively. A first-order explicit Euler scheme as well as a second-order Runge-Kutta scheme are available for time integration. Various approaches are implemented to model surface tension forces, such as the conservative continuous surface stress (CSS) model by Lafaurie et al. [38], the continuum surface force model (CSF) by Brackbill et al. [7], and the balanced force approach by Popinet [47]. The latter is used in this study. Two second order advection methods can be used in FS3D. These are the classical Strang splitting algorithm [82], where three one-dimensional non-conservative transport equations in each direction are applied successively, and also a geometrical unsplit advection scheme, which uses more realistic volume fluxes [53]. A wide range of applications have been addressed with FS3D in the last twenty years (e.g. [62],[64],[20],[71],[27],[54]).

In the following we will describe the new evaporation model. In order to solve the mass and energy conservation, we first treat the convective terms and subsequently all other terms in a consistent phase change loop.

3.1. Advection of fluid and gas

Due to the volume generation at the interface, which is inherent to evaporation, the volume source modifies to $\nabla \cdot \mathbf{u} \neq 0$ in interfacial cells. We combine it with the momentum balance Eq. 8 to solve for the pressure term. Hence, we get the Poisson equation for pressure

$$\frac{\nabla \cdot \mathbf{u} - \nabla \cdot \tilde{\mathbf{u}}}{\Delta t} = \nabla \cdot \left[-\frac{1}{\rho(f_1, f_2)} \nabla p \right]. \quad (15)$$

Here, $\tilde{\mathbf{u}}$ is a temporary velocity including the effect of all forces except the pressure. Note, that this equation is an extended version of the incompressible form because of the volume source term $\nabla \cdot \mathbf{u}$. Two multigrid methods are implemented to solve the set of resulting equations. The first one uses a Red Black Gauss Seidel algorithm for smoothing and can be run in V- or W-cycle schemes [61]. The second one is the recently integrated software package UG4,

originally developed by the group of Wittum [93, 13], located at the Goethe Center for Scientific Computing at the Goethe University in Frankfurt. A great challenge of the numerical approach is, to obtain the strongly different velocities of both phases in interface cells. Due to the VOF-method they have to be derived from only one single averaged velocity which we get from solving the momentum equation. Thus, in the following, we present two alternative methods to calculate consistently the volume source first and subsequently the velocities of both phases. In both cases, the mentioned velocities are avoided in the expression for the volume source, and contrary to previous approaches, there is no need to distribute a velocity divergence error. First, we note that the velocity obtained by solving the momentum equation is mass averaged. In our first proposed solution, the average is formed with the volume fraction of the liquid. This method was developed by Ma and Bothe [42]. Volume- and mass-averaged velocities are defined at the center (superscript c) of the interface cell:

$$\mathbf{u}^c = \frac{f_1 \rho_l \mathbf{u}_l^c + (1 - f_1) \rho_{gp} \mathbf{u}_{gp}^c}{f_1 \rho_l + (1 - f_1) \rho_{gp}} \quad (16)$$

$$\mathbf{u}_{vol}^c = f_1 \mathbf{u}_l^c + (1 - f_1) \mathbf{u}_{gp}^c \quad (17)$$

According to Eq. 12, the relative velocity is given by:

$$\mathbf{u}_{rel}^c = \mathbf{u}_l^c - \mathbf{u}_{gp}^c = \dot{m}'' \left(\frac{1}{\rho_{gp}} - \frac{1}{\rho_l} \right) \mathbf{n}. \quad (18)$$

We assume that the mean velocities of both phases in the considered cell \mathbf{u}_{gp}^c and \mathbf{u}_l^c are equal to their values at the interface. From this set of equations, one obtains the velocities of both phases:

$$\mathbf{u}_l^c = \mathbf{u}^c + \frac{(1 - f_1) \rho_{gp}}{\rho} \mathbf{u}_{rel}^c \quad (19)$$

$$\mathbf{u}_{gp}^c = \mathbf{u}^c - \frac{f_1 \rho_l}{\rho} \mathbf{u}_{rel}^c \quad (20)$$

and the relation between volume- and mass-averaged velocities, assumed constant in the interface cells, is given by

$$\mathbf{u}^c = \mathbf{u}_{vol}^c + \frac{f_1 (1 - f_1) (\rho_l - \rho_{gp})}{\rho} \mathbf{u}_{rel}^c. \quad (21)$$

Henceforth, further approximations are made. In fact, we need the velocities at cell faces, and only the component in the direction perpendicular to them. For this purpose, the component of the velocities \mathbf{u}_{gp}^c and \mathbf{u}_l^c , actually defined at the center of gravity of the PLIC interface, are averaged at the cell faces. First we assume that the velocity vector \mathbf{u} is obtained by averaging the velocities \mathbf{u}^c of two adjacent cells. Subsequently, we take the mean value of the quantities containing \mathbf{u}_{rel}^c , in the direction normal to the considered face. For instance,

the first component in x -direction for the obtained velocities read:

$$u_l = u + \overline{\dot{m}'' \frac{(1-f_1)\rho_{gp}}{\rho} \left(\frac{1}{\rho_{gp}} - \frac{1}{\rho_l} \right) \frac{n_x}{|n|}} \quad (22)$$

$$u_{gp} = u - \overline{\dot{m}'' \frac{f_1\rho_l}{\rho} \left(\frac{1}{\rho_{gp}} - \frac{1}{\rho_l} \right) \frac{n_x}{|n|}}, \quad (23)$$

with the norm definition $|n| = |n_x| + |n_y| + |n_z|$. The overbar denotes the arithmetic average at the cell face from both quantities in neighboring cells.

Taking the divergence of Eq. 21, with $\nabla \cdot \mathbf{n} = \kappa$ and using the current approximation

$$\nabla \cdot \mathbf{u}_{vol} = \dot{m}''' \left(\frac{1}{\rho_{gp}} - \frac{1}{\rho_l} \right) \quad (24)$$

one obtains the final expression

$$\nabla \cdot \mathbf{u} = \dot{m}''' \left(\frac{1}{\rho_{gp}} - \frac{1}{\rho_l} \right) + \frac{f_1(1-f_1)(\rho_l - \rho_{gp})}{\rho} \left(\frac{1}{\rho_{gp}} - \frac{1}{\rho_l} \right) \dot{m}'' \kappa. \quad (25)$$

We propose a second method, assuming that \mathbf{u} is actually averaged with the wetting w_x at cell face. An explaining illustration of the wetting in a cell is shown in B.18. It can be written exemplary for the x -direction:

$$u = \frac{w_x \rho_l u_l + (1-w_x) \rho_{gp}^x u_{gp}}{\rho_x}, \quad (26)$$

ρ_{gp}^x and ρ_x have to be calculated at the cell faces from the densities of the pure phases and the wetting. More precisely:

$$\rho_{gp}^x = \frac{w_{2x} \rho_v + (1-w_x - w_{2x}) \rho_g}{1-w_x} \quad (27)$$

with $w_{2x} = \frac{f_2}{1-f_1}(1-w_x)$ and $\frac{f_2}{1-f_1}$ the averaged vapor volume fraction in the gaseous phase.

The component of the relative velocity in the same direction is obtained by:

$$u_l - u_{gp} = \overline{\left(\frac{1}{\rho_{gp}} - \frac{1}{\rho_l} \right) \dot{m}'' n_x}, \quad (28)$$

where the right-hand-side is again a weighted average at the cell face, from both quantities at the interface in neighboring cells. Solving equations Eq. 26 and Eq. 28, one obtains u_l and u_{gp} as a function of u .

This method is combined with the volume source term calculated in Appendix B, which results in the equation:

$$\iiint \nabla \cdot \mathbf{u} d\Omega = \left(\frac{\rho_{gp}\rho_l}{S_{plic}} \right) \left(\frac{1}{\rho_{gp}} - \frac{1}{\rho_l} \right) \dot{m} \cdot \left[\frac{(w_x^- - w_x^+) n_x dydz}{\rho_x^- \rho_x^+} + \frac{(w_y^- - w_y^+) n_y dx dz}{\rho_y^- \rho_y^+} + \frac{(w_z^- - w_z^+) n_z dx dy}{\rho_z^- \rho_z^+} \right]. \quad (29)$$

Here S_{plic} is the area of the reconstructed interface and $\dot{m} = \dot{m}'' S_{plic}$. For consistency, the velocity is averaged with the wetting at cell faces as well. Moreover, we assume a plane interface in the neighborhood of the cell, therefore, velocities \mathbf{u}_{gp} and \mathbf{u}_l are constant in space for both phases.

The advection of both VOF variables is now conducted using the extracted velocities \mathbf{u}_l and \mathbf{u}_{gp} . Note that the latter is the averaged convective velocity of the gaseous phase. We advect the liquid phase using the Strang splitting scheme [82], thus, three one-dimensional non-conservative transport equations are solved successively. The divergence correction is applied to achieve $f_1 = 1$ inside the fluid and $f_1 = 0$ in the gaseous phase. However, in interfacial cells it generates additional liquid mass because the velocity field is not divergence free. Thus, after the three advection steps in all directions we remove the divergence correction in these cells.

Due to the ideal mixture assumption of vapor and gas a complex advection with geometrical fluxes of the vapor phase is not necessary. Therefore, the fluxes are taken from the product of the wetting w and velocities \mathbf{u}_{gp} , which yields

$$\mathbf{F}_{gp} = (1 - w)\mathbf{u}_{gp}. \quad (30)$$

Actually we convect the volume fraction of vapor in the gaseous phase, which is the ratio of $f_2/(1 - f_1)$. Following the approach of Schlottke [71] we use the TVD-Limiter of Van Leer [92] in order to interpolate the values of the mentioned ratio onto the cell edges. For the temperature advection of T_l and T_{gp} we take the same volume fluxes as for the VOF variables f_1 and f_2 , respectively. Correspondingly, the interpolation of the temperatures is achieved.

3.2. Phase change algorithm

The phase change algorithm is partly based on the proposed numerical solution scheme of Reitzle et al. [54] and is considerably modified and extended to account for evaporation processes. We point out, that the here presented algorithm differs strongly from the original method [54], which accounts solely for sublimation processes. This is obviously a consequence of the different character of evaporation processes. Especially higher evaporation rates, leading to a larger Stefan flow, play a crucial role and enhance non-linear effects. Hence, a fully consistent treatment of the conservation equations is indispensable. Furthermore, the handling of the moving liquid interface is, in contrast to the fixed interface of sublimation processes, an additional challenge, which has to be issued.

The basic concepts of the evaporation process are visualized for a droplet in Fig. 1. The involved quantities of the heat and mass transfer are depicted and named. The retraction of the interface due to evaporation is indicated as a dotted line. The coupling between the VOF-variables and the temperature is mainly achieved via the interface temperature. The latter is used first to calculate the saturated vapor pressure at the interface, which is done by using the Wagner Eq. 14, and subsequently the vapor fraction. The growth velocity is then calculated from the vapor fraction gradient. Secondly, the interface

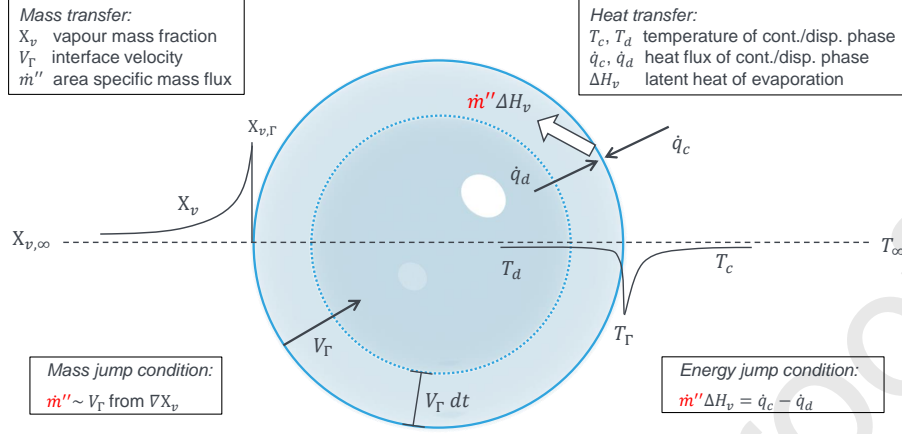


Figure 1: Sketch of an evaporating droplet with the relevant involved quantities. The coupling between heat and mass transfer is achieved via the jump conditions. The retraction of the interface due to evaporation is shown as a dotted line.

temperature is calculated consistently from the energy jump condition from Eq. 13. Diffusion equations for vapor concentration and temperature are solved implicitly, incorporating the corresponding source terms \dot{q}''' and \dot{m}''' as Dirichlet boundary conditions at the PLIC surface. The results are monotone temperature and concentration fields, and, in contrast to a previous treatment, where the sources were first put in the interface cells where they are calculated, and physical diffusion was carried out afterward, such that an ad-hoc redistribution of the source is not necessary.

To achieve this coupling we make use of a fully consistent loop. Convergence is controlled regarding the growth velocity when the residual for an iteration $m + 1$ is smaller than a threshold value ε_Γ , which is set to a value of 10^{-6} . The equation for the residuum reads

$$res = \frac{1}{N_\Gamma} \sum_{N_\Gamma} \left(1 - \frac{V_\Gamma^m}{V_\Gamma^{m+1}} \right) \leq \varepsilon_\Gamma, \quad (31)$$

where N_Γ denotes the number of interface cells. In addition, V_Γ is underrelaxed in order to gain successful convergence. In the investigated cases described in the following sections the average number of iterations of the evaporation loop is between 8 and 12, strongly dependent on the simulation setup. Thus, the computational costs are higher than with our old model but still in an acceptable range. The whole numerical procedure of the evaporation loop is depicted in Fig. 2. Note, that the convective transport has already been done outside the phase change loop (described in the previous subsection). Additionally, the evaluation of the jump conditions as well as the heat conduction is part of the loop. In contrast to sublimation [54], this is necessary to achieve convergence, due to the higher amount of vapor produced at evaporation processes. Another important element of the loop, which is required due to the retraction

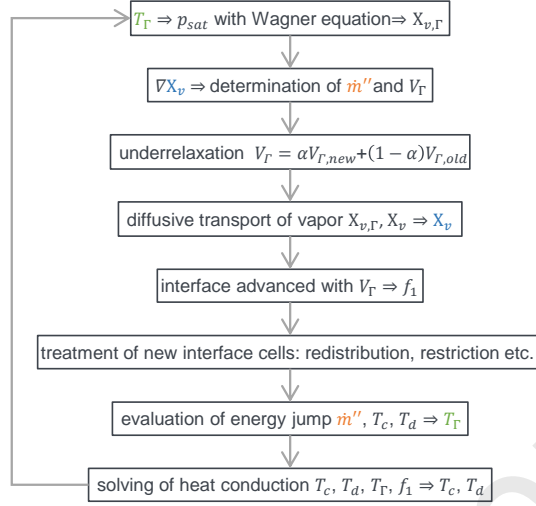


Figure 2: Numerical algorithm of the evaporation loop. The loop is stopped when convergence is achieved.

of the interface, is the treatment of emerged, interfacial cells. When dealing with higher evaporation rates, it is possible that the growth velocity during an iteration is large enough to affect cells, which are completely filled with the disperse phase ($f_1 = 1$) and lie in the vicinity of the interface. In this case an algorithm is applied, which first detects the involved cells and in a second step evaluates the amount of the corresponding evaporated mass. According to the simulation problem and the ambient conditions a threshold value is estimated. Based on this value and the wetting of the surrounding cells the algorithm decides, whether the evaporated amount is redistributed to neighboring cells or the corresponding cell is treated as a new interface cell. The redistribution is applied, in order to gain conservation of mass on the one hand side and on the other hand side to prevent generation of embedded interface cells. The latter would lead to an unsteady interface with overlapping PLIC surfaces, which then results the generation of evaporating cells beyond the interface inside the liquid. In consequence this leads to a formation of "holes" in the vicinity of the interface and finally to an unstable simulation. This behavior is one reason for the deviations in previous simulations with high evaporation rates [71]. When a cell is detected and determined as a new interface cell, the temporary interface temperature T_Γ as well as the continuous temperature T_c are interpolated from a weighted 27-stencil of the surrounding interface and continuous cells, respectively. The vapor mass fraction is subsequently calculated with the saturation pressure following the above mentioned procedure.

After the evaporation loop we calculate the volume specific mass source \dot{m}''' from the change in the volume fraction f_1 due to the retraction of the interface with the growth velocity. Finally, the source of the Poisson equation of

pressure, 15, is derived from this value.

4. Validation

Due to the complexity of DNS with phase change we choose a multistage procedure for the validation of the method. Thus, we will present several validation cases in this section in order to proof the correctness of the implementation and estimate the capability of the new method to simulate evaporation processes with FS3D. We will compare our numerical simulations with available analytical solutions from literature as well as with experimental data and resulting correlations. Furthermore, we consult the previous implemented and validated evaporation models of the code and make a detailed comparison. Emphasis is put on the validation of attributes regarding phase change, such as evaporation rates, Sherwood numbers (Sh), or vapor field fractions. Extensive validation cases of the code concerning other aspects, e.g. advection, surface tension, transient heat transfer, or purely fluid dynamic features, have been conducted in the last decades and are not part of this study. The reader is referred to the respective literature [61, 11, 28, 71, 54]. All validations are conducted on a three-dimensional Cartesian grid. Extensive grid refinement studies have been performed for all presented validation cases, however, we will show only for the second case a brief extract exemplarily.

4.1. Evaporation in a Couette flow

For the first validation case, we consider a fully developed laminar flow between two parallel plates, where the lower plate is wetted with an evaporating fluid film, and the upper one is moved with a constant velocity u_∞ . For high mass-transfer-rates, Kays et al. [36] derive the expression for the conductance as

$$g = \frac{\dot{m}''}{B_M} = g^* \frac{\ln(1 + B_M)}{B_M}, \quad (32)$$

where $g^* = \frac{\rho_{gp} \mathcal{D}_{bin}}{\delta}$ is the low-mass transfer limit $\dot{m}'' \rightarrow 0$, and δ is the distance between the interface and the upper plate. The mass-transfer driving force is defined by

$$B_M = \frac{X_v^{sat} - X_v^\infty}{1 - X_v^{sat}}. \quad (33)$$

The saturated vapor mass fraction at the interface X_v^{sat} is calculated from the surface temperature T_S , which is varied between $273K$ and $368K$. X_v^∞ is the constant vapor mass fraction at the upper plate. Note, that we do not solve the energy equation, thus, T_S is set constant. There are no volume forces \mathbf{g} and \mathbf{f}_γ , whereas viscous stresses in the gaseous phase are considered, as well as the volume source term leading to a Stefan flow, i.e. the velocity component orthogonal to the interface. The thickness of the fluid film is half a cell and kept constant. The whole configuration is a validation for the convection and diffusion of the vapor phase, including the correct implementation of the vapor

458 source term, as a Dirichlet condition at the interface in the diffusion equation.
 459 We assign periodic boundary conditions in flow direction, no slip conditions at
 460 the upper plate and free slip conditions at the side walls. We choose following
 461 values for the numerical setup: The distance between the plates is $\delta_0 = 0.0125$ m,
 462 the grid is equidistant with 64 grid points in flow direction, and 8 in the other
 463 directions. The velocity of the upper plate is $u_\infty = 0.2$ m/s, the diffusion co-
 464 efficient is $\mathfrak{D}_{bin} = 2.645 \cdot 10^{-5}$ m²/s. Furthermore, we assume equal densities
 465 for the vapor and the inert gas, $\rho_{gp} = 1.0$ kg/m³, which is also a constraint of
 466 the analytical solution. The liquid density is $\rho_l = 998.2$ kg/m³. $X_v^\infty = 0$ is set
 467 in the dummy cells of the wall. The results for various mass transfer numbers
 468 are depicted in Fig. 3. The simulations match the analytical solution very well,
 469 thus, the present method is able to calculate the mass diffusion and the Stefan
 470 flow in a correct manner. Solely the last point differs slightly. However, this
 471 point is in the vicinity to the boiling point with very high evaporation rates,
 where non-linear effects play a stronger role.

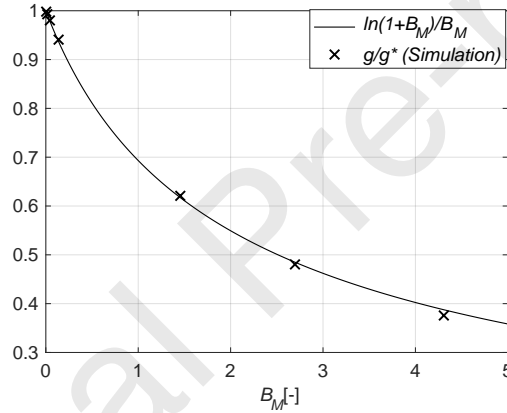


Figure 3: Simulation results for different mass transfer numbers compared with the analytical solution from [36].

472

4.2. Evaporating droplets in an air flow

474 For the second validation case we investigate a droplet in an air flow at
 475 different velocities. The numerical setup, comprising the droplet, an out- and
 476 inflow boundary as well as four lateral free slip conditions, is shown in Fig. 4.
 477 The diameter of the spherical droplet was resolved with 8, 16 and 32 cells. The
 478 distance to the boundaries is chosen in a way, that disturbances and influence of
 479 boundary effects are negligible. The results for all three grids in terms of mass
 480 and heat transfer are in a comparable range. The values for the corresponding
 481 Sherwood numbers as well as the values of the computed grid convergence index
 482 GCI [63] are shown in Table 1. The deviation between the medium and fine
 483 grid is significantly smaller, showing a good convergence. For all other presented

Table 1: Results for the simulation cases with different grid sizes

	Grid	Re = 35	Re = 80	Re = 130
Sh [-]	coarse	4.0	5.1	6.1
Sh [-]	medium	4.6	5.8	6.9
Sh [-]	fine	4.8	6.0	7.1
GCI [%]	fine	2.6	1.6	1.1

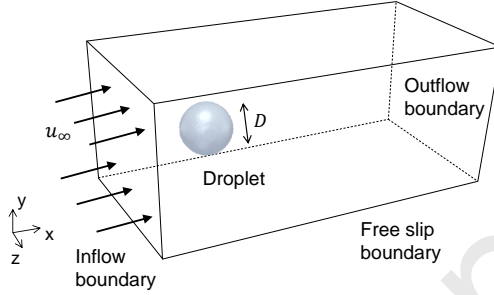


Figure 4: Sketch of the numerical setup of an evaporating droplet in an air flow.

validation cases the same procedure was applied, showing similar behavior. For the validation we compare the computed Sherwood number

$$\text{Sh} = \frac{D\beta}{\mathfrak{D}_{bin}} \quad (34)$$

with D being the volume equivalent diameter of a droplet and β the mass transfer coefficient. We compare three simulations with the medium grid at different Reynolds numbers (Re) with experimental data from Schwarz and Smolik [72] and with correlations from Ranz and Marshall [50], Kulmala and Vesala [37] as well as Schlottke [68]. Material properties are chosen according to [50]. The Sherwood numbers are taken from a fully converged state of the simulations. This aspect is discussed later in detail, when consulting the old evaporation models of our code. All results are depicted in Fig. 5. The results are in very good accordance with the data from literature. The linear fit of our simulations yields

$$\text{Sh} = 2.012 + 0.498\text{Re}^{1/2}\text{Sc}^{1/3}. \quad (35)$$

Note, that due to the low number of simulations this should not be seen as a new correlation, but more as a confirmation of the improvement and correctness of the new evaporation model. Another aspect can be evaluated when looking at the mentioned temporal evolution of Sh and the comparison to the old models from Hase [25] and Schlottke [68]. Figure 6 is adapted from [71] and complemented with the result of our simulation at the highest Sh. Note, that a quantitative comparison is not part of interest here. The parameters for the simulations are in comparable range but not identical. Thus, the focus is not on the different levels of the converged Sherwood numbers, but rather on the

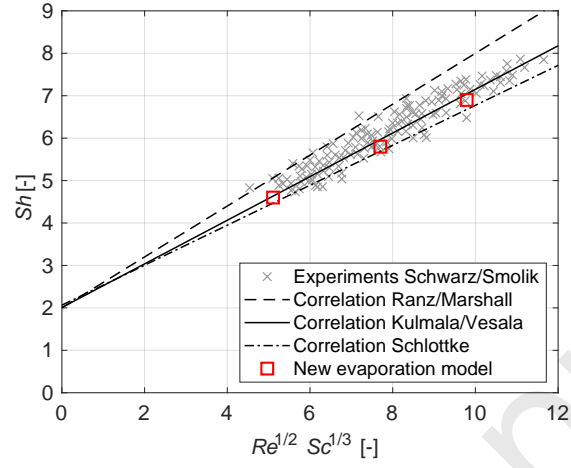


Figure 5: Comparison of Sh for low evaporating droplets in an air flow with experiments from Schwarz and Smolik [72] and correlations from Ranz and Marshall [50], Kulmala and Vesala [37] as well as Schlottke [68].

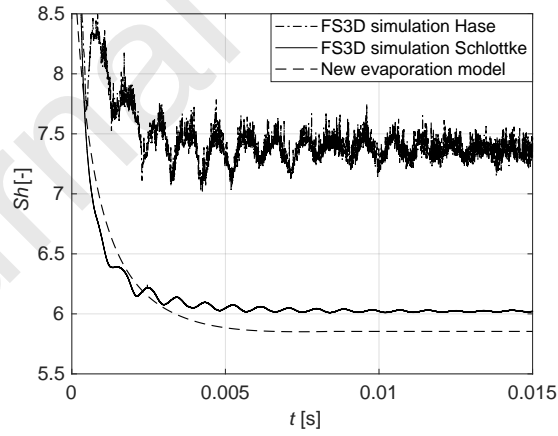


Figure 6: Comparison of the evaporation models from Hase [25] and Schlottke [68] with the new evaporation model. The temporal evolution of the Sherwood number of an evaporating droplet in an airflow is shown.

evolution of the different curves. One can see, that with our current model we obtain a smooth curve whereas for the other models small deviations and fluctuations are present. This improvement is a consequence of the fully consistent evaporation model, which guaranties a well defined smoother behavior in interface cells. Thus, various issues, such as velocity fluctuations, local evaporation peaks due to inaccurate temperature calculations, deviation due to decoupling of neighboring cells, or issues with the source term determination, are improved considerably.

4.3. Evaporation of deformed droplets

In order to validate the calculation procedure of the evaporation loop separately we make a comparison to an analytical solution of evaporating spheroidal drops developed by Tonini and Cossali [85]. They investigated the evaporation rate as well as the vapor and temperature distribution in the whole gaseous phase. They assume constant temperature at the interface of the droplet. Thus, we simulate a prolate and an oblate droplet following the mentioned paper. We introduce the ratio of the radial and axial semi-axes of an ellipsoid $\varepsilon = \frac{a_z}{a_r}$ ($\varepsilon < 1 \rightarrow$ oblate; $\varepsilon > 1 \rightarrow$ prolate) and choose a medium deviation of $\varepsilon_{oblate} = 0.49$ and $\varepsilon_{prolate} = 2.22$. The analytical solution accounts for non-moving stable shapes, therefore, in order to apply similar conditions we switch off the advection of fluid described in section 3.1. Hence, we get a good evaluation of the purely phase change algorithm. The simulations of both droplets, which have the same volume, are performed on a 128^3 grid. The evaluation takes place after a certain time, when the change in the total amount of the vapor fraction field between two time steps is below 10^{-7} . Therefore, we assure a sufficient converged state, which obviously can't be achieved in a spacial limited DNS. Figure 7 shows the comparison of the vapor field distribution of the simulation (left) and the analytical solution (right). The latter is extracted without modification from [85]. One can see, that the visual comparison of the vapor field is in nearly perfect accordance. Even though it is a 3D simulation on a Cartesian grid, the distribution of the vapor around the droplet has a very smooth evolution. Solely in few interface cells we get a little staggered behavior, however, there is no noticeable influence on the whole vapor distribution. In order to get also a quantitative analysis, we investigate the dimensionless local vapor flux η_{vap} directly along the drop surface. In the frame of the above mentioned study Tonini and Cossali [85] derived an analytical solution for the prolate and the oblate droplet. They observed an influence of the local curvature on the vapor flux, the higher the curvature the higher the evaporation rate. Figure 7 depicts the local vapor flux profile along the drop surface for the analytical solution and the simulations of both droplet shapes. Due to the few small mentioned fluctuations of the vapor flux in the simulation we computed the average value in 9° steps of the rotational 3D angle starting from the center of mass of the droplet. The average points are plotted with $+$ symbols for the prolate and with \times symbols for the oblate simulation, respectively. Even for this very sensitive analysis our evaporation model provides accurate values,

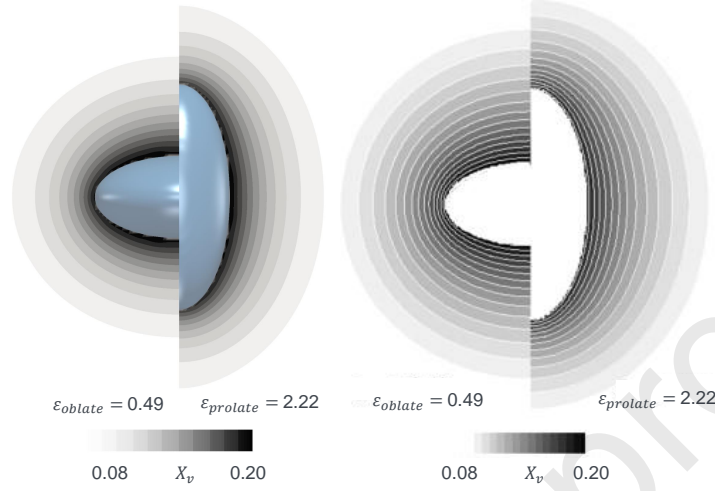


Figure 7: Comparison of the vapor field around a prolate ($\varepsilon_{prolate}$) and an oblate (ε_{oblate}) droplet. On the left the 3D simulation with FS3D is depicted, on the right side the analytical solution of Tonini and Cossali [85] is shown.

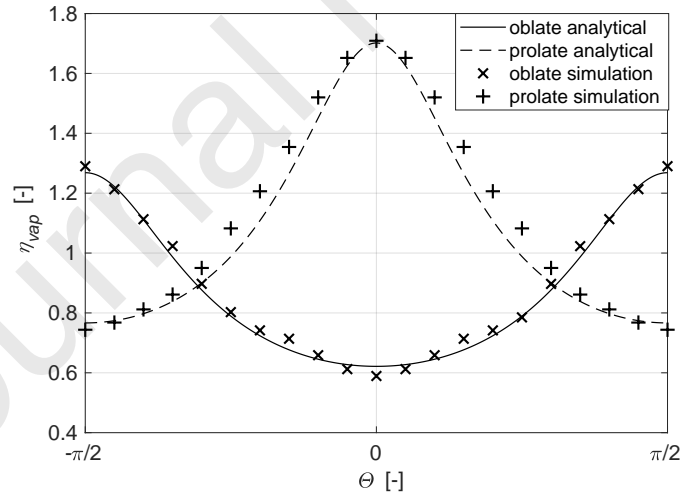


Figure 8: Comparison of the analytical solution [85] and the simulation with the new evaporation model. The non-dimensionalized evaporation rate over the angle of a prolate and an oblate droplet with same volume are shown.

549 which agree with the analytical solution. Small deviations can be affiliated to
 550 the complex surface reconstruction on a Cartesian grid and numerical issues.

551 4.4. Evaporation of a levitated droplet with high evaporation rates

552 In a next step we present a simulation of an evaporating levitated droplet in
 553 a high pressure and temperature environment. On the one hand we investigate
 554 the behavior concerning the stability of the droplet in the domain and of the
 555 surface during evaporation. A complete quiescent ambiance is a big issue for
 556 DNS calculations due to the development of spurious currents. On the other
 557 hand we want to validate the correctness of the temperature and vapor flux at
 558 high evaporation rates. The numerical setup is based on our previous published
 559 work, where we presented preliminary results of the new evaporation model [81].
 560 A levitated n-hexane droplet in a nitrogen atmosphere at $p_{atm} = 60$ bar, $T_{atm} =$
 561 $T_{drop} = 473.15$ K and a concentration in the far field of $x_{atm,N_2} = 0.9979$
 562 is simulated. The whole simulation time is set to 0.5 s, thus, we ensure that
 563 possible numerical effects at the beginning of the simulation are overcome. They
 564 arise mainly due to the very high gradients due to the initialization conditions.
 565 The droplet diameter is chosen in a way, that the final diameter reaches a value
 566 of about $1.25 \cdot 10^{-3}$ m. The results are compared with well known analytical
 567 evaporation models of Gyarmathy [22] and Young [98]. For both analytical
 568 models we consider approaches without and with solubility effects of the inert
 569 gas into the fluid. For a detailed discussion regarding the model approaches and
 570 the selection of the evaporation models we refer to Lamanna et al. [39]. Note
 571 that in our model solubility effects are neglected.

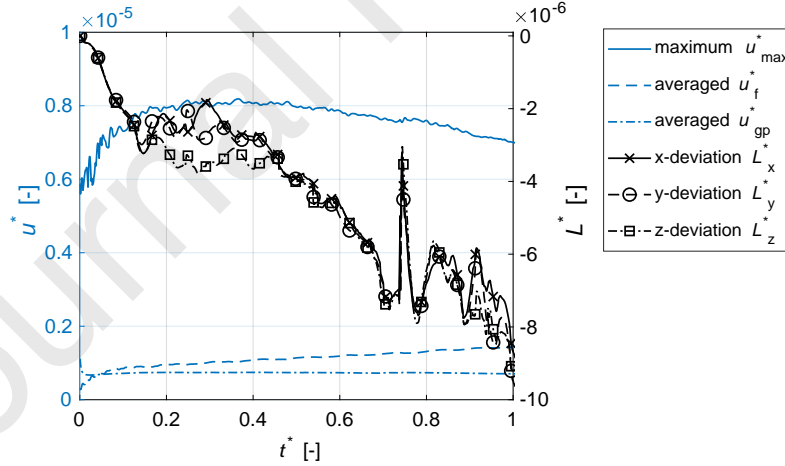


Figure 9: Evolution of the dimensionless deviation L^* of the center of mass and the dimensionless velocity u^* of the levitated evaporating droplet over time t^*

572 For the evaluation of the numerical stability of simulations for high evap-
 573 oration processes we introduce the dimensionless velocity $u^* = \rho D_{drop} u / \mu$. It

is calculated for the maximum occurring velocity of every time step and for the volume average velocity of the whole liquid and gaseous field. Therefore, a good indicator for the stability of the simulation. Furthermore, we define the dimensionless deviation L^* , which is the relation of the distance from the initial position of the droplet and the domain length in each direction. Figure 9 shows the resulting curves for both parameters over the total dimensionless time $t^* = t/t_{end}$ of the simulation. The velocities show a very stable behavior with only small occurring maximum velocities. The volume average fluid velocity increases, which is certainly a consequence of the retracting interface due to evaporation. The deviation of the droplet from the initial center of mass shows also a good trend. Even for the long time for DNS standards, the droplet actually stays in the middle of the domain. All investigated parameter were orders of magnitude higher for simulations with our old models, hence, the numerical stability could be improved considerably. In terms of heat and mass transfer

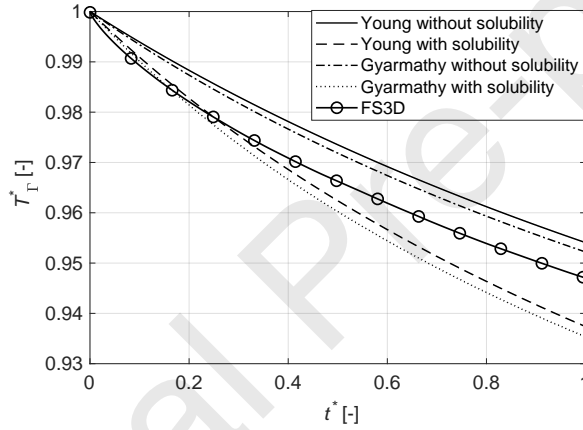


Figure 10: Evolution of the dimensionless surface temperature T_Γ^* of a levitated n-hexane droplet in a nitrogen atmosphere at $p_\infty = 60$ bar, $T_\infty = 473.15$ K, $T_{drop} = 473.15$ K and $x_{\infty, N_2} = 0.9979$. The simulation is compared with analytical models from Gyarmathy [22] and Young [98]

we take a look at the evolution of the droplet surface temperature T_Γ^* as well as the diameter D^* . Both quantities are normalized with the initial respective value. Figure 10 and Figure 11 show the graphs for the simulation with FS3D and both analytical models with and without solubility effects. The overall trend shows a reasonable agreement between the numerical and analytical results. The deviation at the beginning can be attributed to the mentioned numerical initialization. However, at a later stage the overall trend of the slopes are comparable. Particularly, when looking at the models without solubility. Nevertheless, when considering solubility effects at high evaporation rates the method is stretched to its limit.

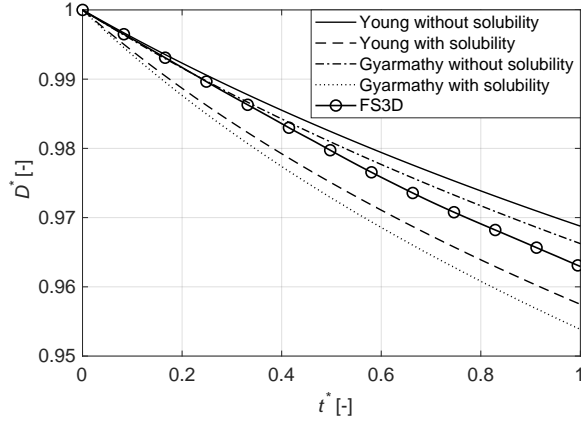


Figure 11: Evolution of dimensionless diameter D^* of a levitated n-hexane droplet in a nitrogen atmosphere at $p_\infty = 60$ bar, $T_\infty = 473.15$ K, $T_{drop} = 473.15$ K and $x_{\infty, N_2} = 0.9979$. The simulation is compared with analytical models from Gyarmathy [22] and Young [98]

5. Results

In the following section we present three simulation setups at different initial and ambient conditions, in order to demonstrate the power of our new evaporation model. We start with a study of supercooled droplets at various temperatures and humidities. In a second step we investigate oscillating droplets with higher evaporation rates and evaluate the behavior in terms of oscillation modes and the comparison with a non-evaporating droplet. Finally, we show a simulation of a falling droplet in a high temperature and pressure environment. All simulation are conducted on a 3D Cartesian grid. Thus, we cover many important aspects for a DNS method capable of simulating evaporation processes. These are for example very low and very high temperature regimes and evaporation rates, considering non-linear effects, strong deformation of the interface or behavior in complex flow fields.

5.1. Supercooled water droplets at subzero temperatures and varying humidity

Supercooled droplets exist at sub-zero temperatures and are present in clouds at high altitude. Evaporation processes of those droplets are important to understand weather phenomena, such as snow or hail. We simulate water droplets at two ambient temperatures of $T_\infty = 268.15$ K and $T_\infty = 253.15$ K. The relative humidity is varied between 0 and 75 %. We compare the evaporation rates of the different settings with simulation using our old evaporation model and with experiments conducted by Ruberto et al. [65]. For these extreme ambient conditions a very precise simulation is indispensable in order to cope with the very low evaporation rates and the small differences between the settings. The numerical setup is similar to the one described in Sec 4.2. Solely the droplet

Table 2: Comparison of evaporation rates of supercooled droplets at different temperatures and humidities

T_∞ [K]	Humidity	Evaporation rate β [μm]			
		Experimental fit Ruberto [65]	D^2 - model	Old model	New model
268.15	0.00	388.1	389.3	416.7	390.2
	0.25	291.1	292.0	291.1	289.9
	0.50	194.1	194.7	192.2	189.3
	0.75	97.0	97.3	103.1	96.2
253.15	0.00	157.0	140.3	156.7	149.8
	0.25	117.8	105.2	128.3	112.4
	0.50	78.5	70.2	86.6	75.1
	0.75	39.3	35.1	48.2	37.5

diameter and the dimensions as well as the material properties are adapted. The latter are adjusted from the mentioned experiments. Table 2 shows the result for the eight performed simulations as well as the experimental fit, the classical D^2 -model [44] estimations, and the simulation results of the old evaporation model. One can see that the simulations with our new model are in very good agreement. For both temperature regimes and the varying humidities the maximum deviations from the experimental fit is about 5 %, from the classical D^2 -model about 7 %. However, the difference between the latter and the experiments are in the same order of magnitude. Noteworthy is also the ability of the old model, which is also very reliable for very low evaporation rates.

5.2. Oscillating droplet with high evaporation rates

In the following we present two simulations of an oscillating water droplet at $T_{H_2O} = 353.1$ K with and without evaporation. The ambient air has the same temperature and a pressure of $p_{amb} = 1.013$ bar. The droplet has a mass of $m = 2.8093 \times 10^{-7}$ kg and is initialized as an ellipsoid with a deviation of 20 % from the spherical shape. Hence, the half axes of the initial ellipsoidal droplet are $1.2a_x = 1.2b_y = c_z$. The simulations are performed on a 256^3 cells grid with continuous boundary conditions on each side. The droplet is positioned in the middle of the domain, the distance to the boundaries is sufficient to prevent unwanted boundary effects. For the evaluation we make use of the recently implemented method for extracting oscillation modes based on a spectral decomposition into Legendre polynomials [59]. We point out, that the high resolution is a necessity of this extraction method and not implicitly required for the evaporation part of the simulation. We introduce the Legendre coefficients A_{km} , which represent the respective modes $m = 1, 2, \dots$ of the droplet oscillation. Furthermore, we define the dimensionless surface area A^* as the ratio of the current droplet surface in time and the initial surface area of the ellipsoid, and the dimensionless time t_{osc} , which is the time for one oscillation of a non-evaporating droplet. For details regarding the extraction of the Leg-

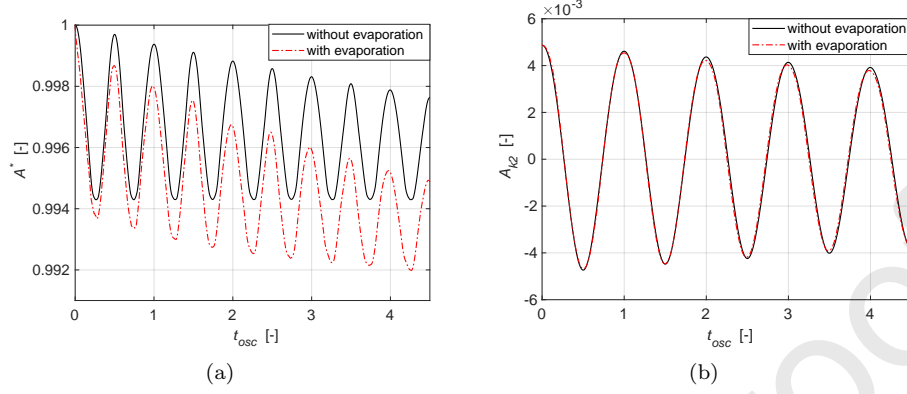


Figure 12: Droplet oscillation without and with high evaporation. The dimensionless area evolution (a) as well as the second oscillation mode (b) is plotted over time

652 endre coefficients, the analytical approach of the method and the validation the
 653 reader is referred to the mentioned literature [59]. In a first step we compare
 654 the evolution of the areas of both simulations, with and without evaporation.
 655 Figure 12 (a) shows the curves of A^* over time t_{osc} . As expected, the total
 656 surface area has a sinusoidal character with peaks, when the droplet reaches the
 657 maximum oblate or prolate state, and troughs during the spherical state. Both
 658 simulations are damped, which is a consequence of the viscous forces. Further-
 659 more, the simulation with evaporation decreases due to the mass loss in the
 660 liquid phase inherent to phase change. However, the frequency increases due
 661 to the smaller radius. This is accompanied by the temporal evolution of the
 662 evaporation rate. A more detailed evaluation of the oscillation can be achieved
 663 when looking at the different oscillation modes. In Fig. 12 (a) and Fig. 13 the
 664 graphs of the relevant even modes are depicted for both cases. The odd modes
 665 and higher modes are negligible due to the symmetric character of the oscilla-
 666 tion and the fast damping of large modes, respectively. A detailed discussion of
 667 these circumstances can be found in [59] and, thus, they are not reported here.
 668 The second mode, which is the main mode of the oscillation, is almost identical
 669 for both cases. Solely a slightly faster decrease of the peaks and the higher
 670 frequency in the simulation with evaporation can be detected. This behavior of
 671 the second mode is as expected since the evaporation of the droplet has only a
 672 marginal effect on the main oscillation of the droplet. However larger effects can
 673 be seen when considering the fourth and sixth mode. These modes react much
 674 more sensitive on very small changes in the topology of the droplet. Thus, they
 675 are more distinct in the evaporation simulation, which can be seen in Fig. 13.
 676 Note, that in this case the A_{k6} values are slightly noisy at the beginning. The
 677 reason for that is probably the high sensitivity of the method for smallest inter-
 678 face changes and numerical issues, which are more present when simulating with
 679 evaporation. However, for the regarded order of magnitude of the higher modes

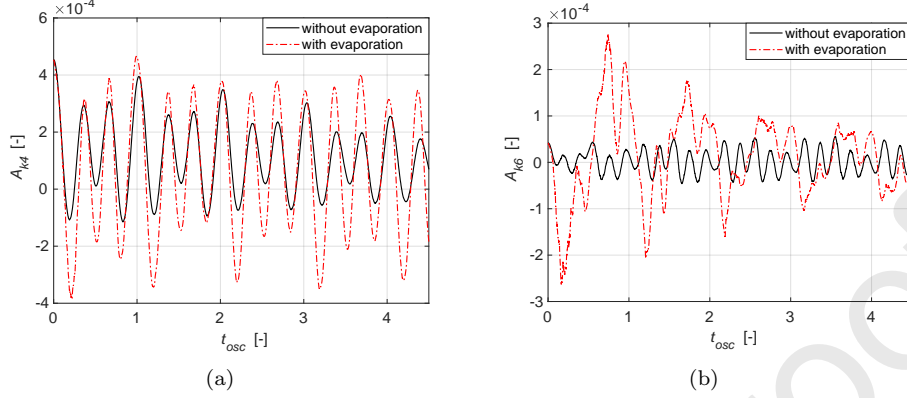


Figure 13: Droplet oscillation without and with high evaporation. The fourth (a) and sixth (b) oscillation mode is plotted over time

Table 3: Dominant frequencies of the coefficients A_{k2} , A_{k4} and A_{k6} obtained from an FFT analysis. The values for the simulations with and without evaporation as well as an analytical solution from Lamb [40] is shown.

Frequencies [Hz]	A_{k2}	A_{k4}	A_{k6}
Without evaporation	472.3	1416	2606
With evaporation	474.5	1423	2622
Lamb	468.8	1407	2568

this is still reasonable. Subsequently, we evaluate the calculated graphs of the Legendre coefficients using FFT in order to obtain the dominant frequencies of the modes. Additionally, we compare them to an analytical model for oscillating droplets from Lamb [40]. The analytical solution for the angular frequency reads

$$\omega^2 = \frac{m(m-1)(m+2)}{\frac{\rho_a}{\rho_l}m + (m+1)} \frac{\sigma}{\rho_l R_0^3}, \quad (36)$$

where R_0 denotes the volume equivalent radius of a sphere. The frequencies of the FFT are shown in Table 3. As expected, all frequencies of the simulation with evaporation are slightly larger and the higher the modes the higher the deviations. An additional investigation of the temporal damping behavior of this simulation over every single oscillation cycle have been conducted, however, the changes of these values are marginal and not part of this study. Both simulation results are in good accordance with the analytical solution. Note, that the analytical solution basically accounts for very small initial deviations from the spherical shape. The small differences to the simulations can be attributed to this fact. Further investigations of the influence of evaporation onto the oscillation behavior are planned in the future, especially a comparison to analytical models [87], which consider this effect.

5.3. Free falling droplet under high pressure and temperature conditions

One of the most challenging cases for a DNS code constitutes a setup comprising very strong deformation of the interface, high velocities and internal flows in combination with high evaporation rates. Thus, we present a simulation of a droplet, which is initially deformed and falls freely due to gravitational forces while evaporating in a high pressure and temperature ambience. In order to evaluate the simulation and ensure physical comparability, the setup is adapted to experiments of Bork et al. [6], conducted in a high pressure chamber. A preliminary simulation with our old evaporation model of this case has been performed and published in [81]. We use the same numerical initialization, depicted in Fig. 14. It comprises a partly cut ellipsoidal droplet at the top wall (free slip boundary) with an initial velocity, measured from the experiments. Previous studies showed, that this setup describes the droplet behavior in terms of shape, falling velocity, oscillation characteristics and vapor field distribution in an adequate way. The other boundaries are of continuous type. Due to the free falling of the droplet the dimensions of the domain are 24 mm in x -direction and 6 mm in y - and z -direction. The resolution of the three-dimensional Cartesian grid is $512 \times 128 \times 128$ cells. The ambient gas is nitrogen at a pressure of $p_\infty = 60$ bar and a temperature of $T_\infty = 473.15$ K. The droplet has a lower initial temperature of $T_\infty = 440.15$ K, due to the fact, that the droplet in the experiments cools down during the relatively long dwell time when entering the chamber. The evaluation window is also adapted from the experiments and used for the evaluation of the vapor field. The vapor concentration field in the wake

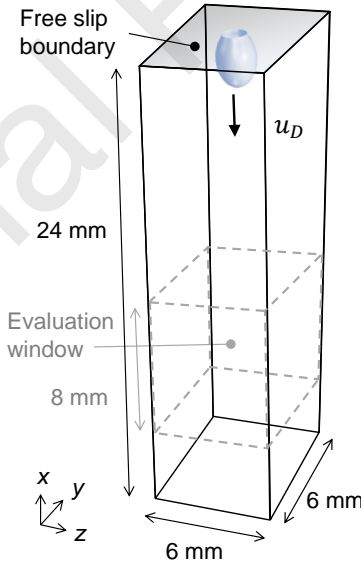


Figure 14: Numerical setup of the falling n-hexane droplet. The initial ellipsoidal droplet is cut at the top wall in order to simulate the falling and oscillation behavior. The evaluation window and all dimensions are taken from the experiments [6].

719 of the droplet is shown in Fig. 15 for both, the simulation on the left and the ex-
 720 periment, taken from [6], on the right side. Note, that this is only a qualitative
 721 comparison, since it is only a selected single shot of one exemplary experiment.
 722 The order of magnitude of the vapor concentration is, however, in reasonably
 723 good agreement. Particularly, the development of vortices in the wake of the
 724 droplet show a comparable behavior. These are a consequence of the droplet os-
 725 cillation, which was compared in preliminary studies, where we investigated free
 726 falling n-pentane droplets in a nitrogen atmosphere in a high pressure ambience.
 727 In a next step we investigate the vapor concentration-temperature profile in the

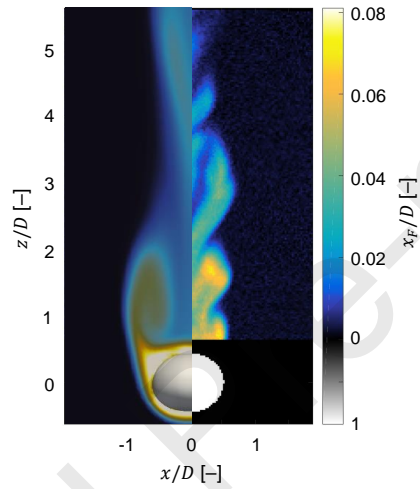


Figure 15: Comparison of simulation with the new evaporation model (left half) and experiments from [81] (right half). Shown are the vapor concentration fields in the wake of a falling n-hexane droplet in a nitrogen atmosphere at $p_\infty = 60$ bar and $T_\infty = 473.15$ K.

728 evaluation window. Therefore, we plot both, the temperature and the corre-
 729 sponding concentrations, for every cell in the mentioned zone. Furthermore,
 730 we take the appropriate estimated data from the Raman-scattering investiga-
 731 tion from [81]. The results for the simulation and the experimental points
 732 are shown in Fig. 16. The experimental data are depicted as black \circ symbols, the
 733 simulation points with gray $+$ symbols. It is obvious, that both coincide well.
 734 Especially in the near vicinity of the droplet, where the temperatures are low
 735 and the vapor concentration high due to evaporation, the simulation predicts
 736 the behavior in a very good manner. Not only the gaseous temperature is of
 737 great interest but also the temperature field inside the droplet. The look inside
 738 the droplet and the interior temperature distribution is hard to measure with
 739 experimental methods and to the best of the authors knowledge for such extreme
 740 conditions no one has done this so far. Thus, simulations are the only way to
 741 access detailed information about the inside and the surface characteristics of
 742 the droplet. Figure 17 shows the temperature fields in the wake of the droplet,
 743

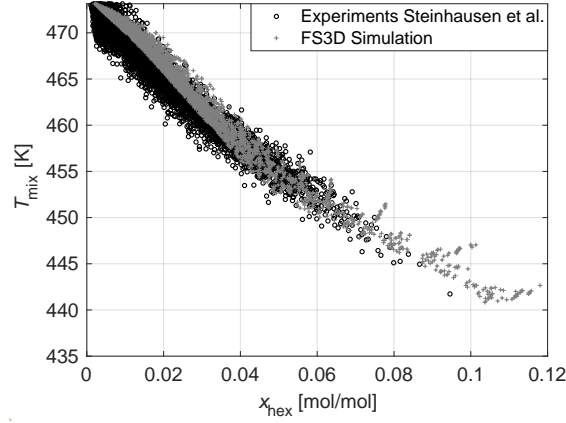


Figure 16: Comparison of numerical vapor concentration-temperature profiles with experimental data from Steinhausen et al. [81] in the wake of a falling n-hexane droplet in a nitrogen atmosphere at $p_\infty = 60$ bar and $T_\infty = 473.15$ K.

on the surface, and inside the droplet for different times $t^* = tu_D/D_0$. Here we have the initial velocity of the droplet u_D and the volume equivalent diameter of a sphere at the beginning of the simulation D_0 . As expected, there is a connection of the temperature field and the above shown concentration field of vapor. We can see also, that the temperature is lower the nearer the distance of the vapor from the droplet surface is. Both, the temperature boundary layer of the droplet and the droplet surface temperature is visible for all times. Conspicuous is the temperature field inside the droplet, which ranges from about 440 K to 434 K. The lowest temperatures are at the surface on the lateral sides of the droplet. Besides, the temperature at the bottom is also in a comparable range. At the top of the droplet we can differ between the prolate-like and the oblate-like shape, where we have lower temperatures for the latter. Remarkable is also the temperature distribution inside the droplet. We can detect, that it is still in the range of the initial droplet temperature of 440 K. Thus, the heat conduction is significantly smaller than the cooling of the surface temperature due to the evaporation process. Additionally, the velocity inside the deformed, oscillating droplet has only a minor influence on the temperature distribution inside the droplet. That is assuming small time periods of the whole falling process of the droplet. In order to evaluate the temperature distribution on the surface we take a look at the experimentally estimated temperature from the experiments in [81]. Here the surface temperature is estimated as the intersection of the extrapolated Raman-scattering estimation and the vapor liquid equilibrium (VLE) line computed with the PC-SAFT [21] equation of state. The estimated temperature for the droplet surface is about 434 K, what agrees very well with the simulation values. Nevertheless, a comparison to real measurements of the surface temperature and the inside distribution would be preferable. The presented simulation shows that our method is able to predict the correct behavior

of evaporating droplets. However, for more extreme conditions we note, that compressible effects might play a major role, which cannot be captured due to the incompressible approach.

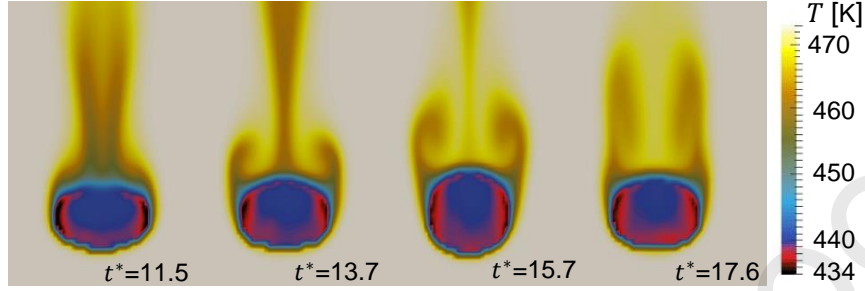


Figure 17: Temperature field inside the droplet and the wake of the n-hexane droplet in a nitrogen atmosphere for different times and droplet shapes during the simulation.

6. Conclusion

A fully consistent method for DNS with evaporation has been presented. The method was implemented into our in-house code FS3D and several validation cases as well as various representative simulations have been conducted. We consulted the corresponding conservation equations as well as the jump conditions and extended them to account for evaporation processes. The new developed framework comprises the advection of the fluid and gaseous phase as well as a fully consistent phase change loop. Furthermore, we showed the relation of the evaporation rate and the growth velocity of the interface during the phase change of the droplet. The physical meaning of the relevant velocities and proposed two methods to extract the velocities for both phases in order to calculate correct physical fluxes has been explained. The same procedure was applied for the temperature advection, where we used a two-field approach containing two temperature fields for both phases, respectively. This allows the right implementation of the energy balance at the interface. The consistent phase change algorithm is necessary especially when dealing with high evaporation rates. It couples heat and mass transfer in a consistent way, thus, the conservation equations are treated interdependently in a closed loop. Implicit handling of diffusion of mass and heat, including the sources at the interface, provide smooth temperature and vapor mass ratio profiles. Convergence is controlled using the relaxed growth velocity. An important part of the described method is the treatment of newly developed interface cells inside the loop, which is a consequence of high evaporation rates. The source for the Poisson equation of pressure is finally calculated with the gained specific volume source during evaporation due to the high density ratio between the phases. Then we presented a multistage validation procedure comprising several cases. In a first step we investigated the correct modeling of the mass diffusion and

the Stefan flow. To this purpose, we set up a Couette flow and compared the mass transfer rates to available analytical solutions. Subsequently, we simulated evaporating droplets in an air flow and compared the Sherwood numbers with experimental data and correlations from the literature. In addition, we consulted our old evaporation models for the same simulations and demonstrated the improvements of the new method. In a next step a comparison has been made of simulations of prolate and oblate evaporating droplets with analytical solutions of the vapor distribution around the droplets. Eventually, we simulated a levitated droplet with very high evaporation rates and showed the ability of the method to cope with extreme conditions and complex setups for DNS. The temperature and diameter evolution of the droplet were compared finally with well known analytical evaporation models from the literature and were in good agreement.

The new evaporation model was then used to simulate various selected cases from very low evaporation rates to high evaporation rates as well as from setups with high deformation and velocities to setups with complete quiescent atmospheres. We started with a simulation series of supercooled droplets at different temperatures and with various ambient humidities. It has been shown that we are able to simulate very low evaporation rates successfully. The results were in good agreement with experimental data and the classical D^2 -model. In a next step we investigated an oscillating evaporating droplet and compared the evolution of the area and different oscillation modes to a droplet without evaporation. In addition, we compared the results with an analytical solution from the literature. Thus, we could observe an influence of evaporation on the oscillation of the droplet. However, further studies concerning this topic have to be conducted and are planned in the near future. Finally, we performed and examined a simulation of a free falling droplet under high pressure and temperature conditions. We proofed the ability of the new evaporation model to deal with very high evaporation rates together with strong surface deformations and high velocities. The simulation was compared to experiments and several aspects, such as the vapor concentration in the wake of the droplet or temperature evolution, and showed good agreement.

The new phase change model is a powerful tool for investigations of various phenomena with evaporation. It can handle extreme ranges of ambient conditions and is able to predict the behavior of evaporating droplets correctly. However, further extensions are planned, comprising fully variable material properties and enhancements in the computational performance of the method.

Acknowledgements

The authors kindly acknowledge the High Performance Computing Center Stuttgart (HLRS) for support and supply of computational time on the Cray XC40 platform under the Grant No. FS3D/11142. Furthermore, the authors kindly acknowledge the financial support by the Deutsche Forschungsgemeinschaft (DFG) within the SFB-TRR75 and the GRK 2160/1. We thank C.

Steinhausen and G. Lamanna for the supply with evaporation models and experimental data, as well as S. Tonini, G.E. Cossali and G. Varma for the active support and the provision of analytical models. Moreover, we acknowledge M. Reitzle and S. Ruberto for numerical, modeling and experimental support.

Appendix A. Mass jump condition

In the following the evaporation rate, growth velocity of the interface due to phase change, and the difference in the velocity of both phases normal to the interface is derived. We start with Eq. 10, which was obtained from the global mass conservation. Furthermore, we consider the conservation of the inert gas and the evaporating substance separately. Hence, we can derive the set of equations

$$\begin{cases} 0 = \rho_{p,g} (u_{g,n} - V_n) \\ \rho_l (u_{l,n} - V_n) = \rho_{p,v} (u_{v,n} - V_n) . \end{cases} \quad (\text{A.1})$$

Here, \mathbf{u}_g and \mathbf{u}_v are the mean velocities of the inert gas and vapor, respectively. The reason for the different values of both velocities is, that they have a convective part related to the mean velocity of the gaseous phase and the diffusive part. Summing up both parts of Eq. A.1 leads to the expressions for the density and fluxes of the gaseous phase:

$$\begin{cases} \rho_{gp} = \rho_{p,g} + \rho_{p,v} \\ \rho_{gp} u_{gp,n} = \rho_{p,g} u_{g,n} + \rho_{p,v} u_{v,n} . \end{cases} \quad (\text{A.2})$$

Now we can calculate the local area specific mass source of vapor \dot{m}'' , which reads

$$\dot{m}'' = -\rho_{p,v} (u_{v,n} - V_n) . \quad (\text{A.3})$$

Using the vapor mass ratio, Eq. 4, and the definition of the Stefan flow $\mathbf{V}_{Sf} = \mathbf{u}_{gp} - \mathbf{V}$, which is defined as the velocity of the gaseous phase relative to the interface, we can calculate \dot{m}'' as the sum of the diffusive and convective part:

$$\dot{m}'' = \mathfrak{D}_{bin} \rho_{gp} \nabla X_v - \rho_{p,v} \mathbf{V}_{Sf} . \quad (\text{A.4})$$

Because there is no flux of the inert gas at the interface we can write

$$\rho_{p,g} \mathbf{V}_{Sf} = \mathfrak{D}_{bin} \rho_{gp} \nabla X_g \quad (\text{A.5})$$

and, finally, the expression for the local area specific mass source of vapor \dot{m}'' results in Eq. 11. From the last two equations we can also derive, that $\dot{m}'' = \rho_{gp} \mathbf{V}_{Sf}$. Thus, this calculation is perfectly consistent with Eq. A.2 and we proofed, that the velocities of the inert gas and vapor are different from the velocity of the gaseous phase due to the opposite diffusive parts. They can be obtained from the above mentioned equations to

$$\begin{cases} \rho_{p,v} u_{v,n} = \rho_{p,v} u_{gp,n} - \mathfrak{D}_{bin} \rho_{gp} \nabla X_v \\ \rho_{p,g} u_{g,n} = \rho_{p,g} u_{gp,n} - \mathfrak{D}_{bin} \rho_{gp} \nabla X_g . \end{cases} \quad (\text{A.6})$$

Furthermore, the jump condition (see Eq. 10) can be directly related to the local area evaporation rate \dot{m}'' :

$$-\dot{m}'' = \rho_l(u_{l,n} - V_n) = \rho_{gp}(u_{gp,n} - V_n) \quad (\text{A.7})$$

Appendix B. Derivation of the volume source term for a plane interface

In the following, the source term Eq. 29 is derived. Fortunately, the expression is independent of the unknown velocities of the inert gas and vapor \mathbf{u}_{gp} and \mathbf{u}_l . Actually, only the known velocity difference proportional to the evaporation rate appears (see Eq. 12). Moreover, a constant density of the gas phase ρ_{gp} (ideal mixture) is assumed. According to Gauss's theorem:

$$\begin{aligned} \iiint \nabla \cdot \mathbf{u} d\Omega &= \iint \mathbf{u} \cdot d\mathbf{S} \\ &= u^+ dydz - u^- dydz + v^+ dx dz - v^- dx dz + w^+ dx dy - w^- dx dy, \end{aligned} \quad (\text{B.1})$$

where the superscripts + and - refer respectively to the largest and smallest component in the corresponding space direction of \mathbf{u} . For cell faces perpendicular to the x -direction, and where velocities (cf. Eq. 26) and densities (cf. Eq. 27) are mass averaged with the wetting, the difference reads:

$$\begin{aligned} u^+ dydz - u^- dydz &= \frac{w_x^+ \rho_l u_l + (1 - w_x^+) \rho_{gp} u_{gp}}{\rho_x^+} - \frac{w_x^- \rho_l u_l + (1 - w_x^-) \rho_{gp} u_{gp}}{\rho_x^-} \\ &= \frac{\rho_{gp} \rho_l (u_{gp} - u_l)(w_x^- - w_x^+)}{\rho_x^- \rho_x^+}. \end{aligned} \quad (\text{B.2})$$

Together with Eq. 12 written in the direction normal to the interface (n_x, n_y, n_z) , where $\dot{m}'' = \frac{\dot{m}}{S_{plic}}$, with S_{plic} being the area of the reconstructed interface, the expression for the source term Eq. 29 is obtained.

Note that, using the volume averaged velocity \mathbf{u}_{vol} , which reads for a cell face perpendicular to the x -direction

$$u_{vol} = w_x u_l + (1 - w_x) u_{gp}, \quad (\text{B.3})$$

similar calculations result in the well-known expression, with the volumetric mass source \dot{m}''' :

$$\iiint \nabla \cdot \mathbf{u}_{vol} d\Omega = \left(\frac{1}{\rho_{gp}} - \frac{1}{\rho_l} \right) \dot{m}'''. \quad (\text{B.4})$$

This can be shown by demonstrating following equation:

$$\frac{(w_x^- - w_x^+) n_x dydz + (w_y^- - w_y^+) n_y dx dz + (w_z^- - w_z^+) n_z dx dy}{S_{plic}} = 1. \quad (\text{B.5})$$

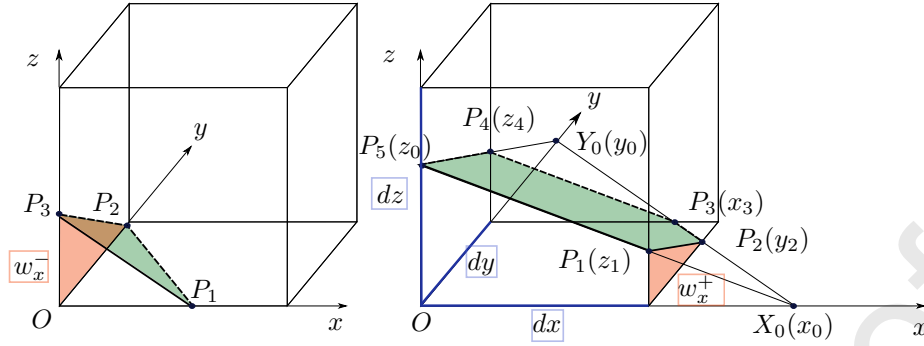


Figure B.18: Configurations for which equality Eq. B.5 is demonstrated (simple case a in the left figure, more complex case b in the right one).

896 We proof this in the following for two configurations of the PLIC surface, shown
 897 in Fig. B.18. In this figure, the system of coordinates with the origin O is shown.
 898 The dimensions of the cell are dx , dy , dz . We filled in the wettings w_x^- and w_x^+
 899 on cell faces orthogonal to the x -direction. The edges of the PLIC surfaces are
 900 labeled with the points P_i .
 901 Now, we consider the simple case in Fig. B.18 (left). First, we define the coordi-
 902 nates of P_i :

$$P_1 = \begin{pmatrix} x_0 \\ 0 \\ 0 \end{pmatrix}, P_2 = \begin{pmatrix} 0 \\ y_0 \\ 0 \end{pmatrix}, P_3 = \begin{pmatrix} 0 \\ 0 \\ z_0 \end{pmatrix}. \quad (\text{B.6})$$

903 The vector normal to the interface \mathbf{n} can be deduced from the cross product
 904 between P_1P_3 and P_1P_2 (which norm is K). It reads in normalized form:

$$\mathbf{n} = \frac{1}{K} \begin{pmatrix} y_0 z_0 \\ x_0 z_0 \\ x_0 y_0 \end{pmatrix} = \begin{pmatrix} n_x \\ n_y \\ n_z \end{pmatrix}. \quad (\text{B.7})$$

905 The interface area is the half of the norm of this cross product, i.e. $S_{plic} = K/2$,
 906 with of course $K^2 = (y_0 z_0)^2 + (x_0 z_0)^2 + (x_0 y_0)^2$.

907 The quantity $w_x^- dydz$ is the wetted area on the cell face located at $x = 0$, thus

$$w_x^- dydz = \frac{y_0 z_0}{2}. \quad (\text{B.8})$$

908 It can be easily shown that (note that $w_x^+ = w_y^+ = w_z^+ = 0$):

$$\begin{aligned} & \frac{w_x^- n_x dydz + w_y^- n_y dxdz + w_z^- n_z dxdy}{S_{plic}} \\ &= \frac{\frac{1}{2} (y_0 z_0)^2 + \frac{1}{2} (x_0 z_0)^2 + \frac{1}{2} (x_0 y_0)^2}{\frac{1}{2} K^2} = 1. \end{aligned} \quad (\text{B.9})$$

909 For case b in Fig. B.18 (right), the interface cuts the x - and y -axis outside of
 910 the cell. First, we define $x' = x_0 - dx$, $y' = y_0 - dy$. Again, we define the
 911 coordinates of P_i :

$$\begin{aligned} P_1 &= \begin{pmatrix} dx \\ 0 \\ z_1 \end{pmatrix}, P_2 = \begin{pmatrix} dx \\ y_2 \\ 0 \end{pmatrix}, P_3 = \begin{pmatrix} x_3 \\ dy \\ 0 \end{pmatrix}, \\ 912 \quad P_4 &= \begin{pmatrix} 0 \\ dy \\ z_4 \end{pmatrix}, P_5 = \begin{pmatrix} 0 \\ 0 \\ z_0 \end{pmatrix}. \end{aligned} \quad (\text{B.10})$$

913 The points of intersection between the PLIC surface and both, the x -axis and
 914 the y -axis:

$$X_0 = \begin{pmatrix} x_0 \\ 0 \\ 0 \end{pmatrix}, Y_0 = \begin{pmatrix} 0 \\ y_0 \\ 0 \end{pmatrix}. \quad (\text{B.11})$$

915 Applying successively the intercept theorem in the triangles $(O X_0 P_5)$, $(O Y_0 P_5)$
 916 and twice in $(O X_0 Y_0)$:

$$\frac{z_1}{x'} = \frac{z_0}{x_0} \quad \frac{z_4}{y'} = \frac{z_0}{y_0} \quad \frac{y_2}{x'} = \frac{y_0}{x_0} \quad \frac{x_3}{y'} = \frac{x_0}{y_0}. \quad (\text{B.12})$$

917 The area of the PLIC interface can be calculated from:

$$S_{plic} = \frac{K}{2} - S_1 - S_2, \quad (\text{B.13})$$

918 with S_1 , S_2 the area of the triangles $(P_1 P_2 X_0)$, $(P_3 P_4 Y_0)$ respectively.

$$S_1 = \frac{1}{2} \left| \begin{pmatrix} y_2 z_1 \\ x' z_1 \\ x' y_2 \end{pmatrix} \right| = \frac{1}{2} \left(\frac{x'}{x_0} \right)^2 \left| \begin{pmatrix} y_0 z_0 \\ x_0 z_0 \\ x_0 y_0 \end{pmatrix} \right| = \frac{1}{2} \left(\frac{x'}{x_0} \right)^2 K, \quad (\text{B.14})$$

919 and similarly

$$S_2 = \frac{1}{2} \left(\frac{y'}{y_0} \right)^2 K \quad (\text{B.15})$$

920

$$S_{plic} = \frac{K}{2} \left(1 - \left(\frac{x'}{x_0} \right)^2 - \left(\frac{y'}{y_0} \right)^2 \right). \quad (\text{B.16})$$

921 The terms containing the wetted areas can be evaluated in the following manner:

$$\begin{aligned} (w_x^- - w_x^+) n_x dy dz &= \left(\left(\frac{z_0 + z_4}{2} \right) dy - \frac{y_2 z_1}{2} \right) n_x \\ &= \left(\left(1 + \frac{y'}{y_0} \right) \left(1 - \frac{y'}{y_0} \right) - \left(\frac{x'}{x_0} \right)^2 \right) y_0 z_0 n_x \\ &= \frac{(y_0 z_0)^2}{2K} \left(1 - \left(\frac{y'}{y_0} \right)^2 - \left(\frac{x'}{x_0} \right)^2 \right), \end{aligned} \quad (\text{B.17})$$

922 and similarly

$$(w_y^- - w_y^+)n_y dx dz = \frac{(x_0 z_0)^2}{2K} \left(1 - \left(\frac{y'}{y_0} \right)^2 - \left(\frac{x'}{x_0} \right)^2 \right), \quad (\text{B.18})$$

923 and for the z-direction:

$$\begin{aligned} w_z^- n_z dx dy &= \left(dx dy - \frac{1}{2} (dx - x_3)(dy - y_2) \right) n_z \\ &= \left(\left(1 - \frac{x'}{x_0} \right) \left(1 - \frac{y'}{y_0} \right) - \frac{1}{2} \left(1 - \frac{y'}{y_0} - \frac{x'}{x_0} \right)^2 \right) x_0 y_0 n_z \\ &= \frac{(x_0 y_0)^2}{2K} \left(1 - \left(\frac{y'}{y_0} \right)^2 - \left(\frac{x'}{x_0} \right)^2 \right). \end{aligned} \quad (\text{B.19})$$

924 Obviously, Eq. B.5 is validated in this case as well. The demonstration is similar
925 for the other configurations.

926 To sum up, the well-known Eq. B.4 for the volume-averaged velocity is recovered
927 with this method, modeling a plane evaporation interface, and the expression
928 is modified to account for a mass-averaged velocity required in the source term
929 for the Poisson equation.

References

- [1] S. K. Aggarwal, F. Peng, A review of droplet dynamics and vaporization modeling for engineering calculations, *Journal of Engineering For Gas Turbines and Power-transactions of the ASME* 117 (3) (1995) 453–461.
- [2] C. Antoine, Tensions des vapeurs: nouvelle relation entre les tensions et les temperatures, *Comptes. Rendus.* 107 (1888) 681–684.
- [3] H. Ban, G. Son, Numerical simulation of droplet evaporation between two circular plates, *Journal of Mechanical Science and Technology* 29 (6) (2015) 2401–2407.
- [4] R. Banerjee, Numerical investigation of evaporation of a single ethanol/isooctane droplet, *Fuel* 107 (2013) 724 – 739.
- [5] M. Birouk, I. Gökalp, Current status of droplet evaporation in turbulent flows, *Progress in Energy and Combustion Science* 32 (2006) 408–423.
- [6] B. Bork, A. Preusche, F. Weckenmann, G. Lamanna, A. Dreizler, Measurement of species concentration and estimation of temperature in the wake of evaporating n-heptane droplets at trans-critical conditions, *Proceedings of the Combustion Institute* 36 (2) (2017) 2433 – 2440.
- [7] J. U. Brackbill, D. B. Kothe, C. Zemach, A continuum method for modeling surface-tension, *Journal of Computational Physics* 100 (2) (1992) 335–354.

- [8] C. Crowe, J. Schwarzkopf, M. Sommerfeld, Y. Tsuji, *Multiphase Flows with Droplets and Particles*, CRC Press, Boca Raton, 2011.
- [9] M. R. Davidson, M. Rudman, Volume-of-fluid calculation of heat or mass transfer across deforming interfaces in two-fluid flow, *Numerical Heat Transfer Part B-fundamentals* 41 (3-4) (2002) 291–308.
- [10] B. Duret, J. Reveillon, T. Menard, F. Demoulin, Improving primary atomization modeling through dns of two-phase flows, *International Journal of Multiphase Flow* 55.
- [11] Eisenschmidt, P. Rauschenberger, C. Rohde, W. B., Modelling of freezing processes in super-cooled droplets on sub-grid scale, in: *ILASS – Europe 2013, 25th European Conference on Liquid Atomization and Spray Systems*, Chania, Greece, 2013.
- [12] D. Enright, R. Fedkiw, J. Ferziger, I. Mitchell, A hybrid particle level set method for improved interface capturing, *Journal of Computational Physics* 183 (1) (2002) 83–116.
- [13] M. Ertl, J. Reutzsch, A. Nägel, G. Wittum, B. Weigand, *High Performance Computing in Science and Engineering '17*, chap. Towards the Implementation of a New Multigrid Solver in the DNS Code FS3D for Simulations of Shear-Thinning Jet Break-Up at Higher Reynolds Numbers, Springer International Publishing, 2017, pp. 269–287.
- [14] G. Faeth, Current status of droplet and liquid combustion, *Progress in Energy and Combustion Science* 3 (4) (1977) 191–224.
- [15] R. P. Fedkiw, T. Aslam, B. Merriman, S. Osher, A non-oscillatory eulerian approach to interfaces in multimaterial flows (the ghost fluid method), *Journal of Computational Physics* 152 (2) (1999) 457–492.
- [16] L. Forero, J. A. Velásquez J., Wagner liquid–vapour pressure equation constants from a simple methodology, *The Journal of Chemical Thermodynamics* 43 (2011) 1235–1251.
- [17] F. Gibou, R. Fedkiw, A fourth order accurate discretization for the laplace and heat equations on arbitrary domains, with applications to the stefan problem, *Journal of Computational Physics* 202 (2) (2005) 577–601.
- [18] J. Glimm, J. Grove, W. Linquist, O. McBryan, G. Tryggvason, The bifurcation of tracked scalar waves, *SIAM Journal on Scientific and Statistical Computing* 9 (1) (1987) 61–79.
- [19] J. Glimm, J. W. Grove, X. Li, N. Zhao, Simple front tracking, *Contemporary Mathematics*.

- [20] H. Gomaa, I. Stotz, M. Sievers, G. Lamanna, B. Weigand, Preliminary Investigation on Diesel Droplet Impact on Oil Wallfilms in Diesel Engines, in: ILASS – Europe 2011, 24th European Conference on Liquid Atomization and Spray Systems, Estoril, Portugal, September 2011, 2011.
- [21] J. Gross, G. Sadowski, Perturbed-chain saft: An equation of state based on a perturbation theory for chain molecules, *Industrial and Engineering Chemistry Engineering Chemistry Research* 40 (4) (2001) 1244–1260.
- [22] G. Gyarmathy, The spherical droplet in gaseous carrier streams: Review and synthesis, *Multiphase Science and Technology* 1 (1-4) (1982) 99–279.
- [23] F. H. Harlow, J. E. Welch, Numerical calculation of time-dependent viscous incompressible flow of fluid with free surface, *Physics of Fluids* 8 (12) (1965) 2182–2189.
- [24] K. Harstad, J. Bellan, An all-pressure fluid drop model applied to a binary mixture: heptane in nitrogen., *International Journal of Multiphase Flow* 26 (2000) 1675–1706.
- [25] M. Hase, Numerische berechnung dreidimensionaler transportvorgänge an angeströmten, sich verformenden tropfen, Ph.D. thesis, Universität Stuttgart (2005).
- [26] M. Hase, B. Weigand, Numerical simulation of 3d unsteady heat transfer at strongly deformed droplets at high reynolds-numbers, *High-Performance Computing in Science and Engineering* (2003) 255–266Springer-Verlag.
- [27] M. Hase, B. Weigand, A numerical model for 3d transient evaporation processes based on the volume-of- fluid method, *ICHMT International Symposium on Advances in Computational Heat Transfer* (2004) 1–23.
- [28] M. Hase, B. Weigand, Transient heat transfer of deforming droplets at high reynolds numbers, *International Journal of Numerical Methods For Heat & Fluid Flow* 14 (1) (2004) 85–97.
- [29] R. J. Haywood, R. Nafziger, M. Renksizbulut, A detailed examination of gas and liquid phase transient processes in convective droplet evaporation, *Journal of heat transfer* 111 (1989) 495–502.
- [30] R. J. Haywood, M. Renksizbulut, G. D. Raithby, Numerical-solution of deforming evaporating droplets at intermediate reynolds-numbers, *Numerical Heat Transfer Part A-applications* 26 (3) (1994) 253–272.
- [31] R. J. Haywood, M. Renksizbulut, G. D. Raithby, Transient deformation and evaporation of droplets at intermediate reynolds-numbers, *International Journal of Heat and Mass Transfer* 37 (9) (1994) 1401–1409.
- [32] C. W. Hirt, B. D. Nichols, Volume of fluid (VOF) method for the dynamics of free boundaries, *Journal of Computational Physics* 39 (1) (1981) 201–225.

- [33] J. M. Hyman, Numerical methods for tracking interfaces, *Physica D: Non-linear Phenomena* 12 (1-3) (1984) 396–407.
- [34] J. John Palmore, O. Desjardins, A volume of fluid framework for interface-resolved simulations of vaporizing liquid-gas flows, *Computational Physics*.
- [35] D. Juric, G. Tryggvason, Computations of boiling flows, *International Journal of Multiphase Flow* 24 (3) (1998) 387–410.
- [36] W. Kays, M. Crawford, B. Weigand, *Convective heat and mass transfer*, 4th ed., McGraw-Hill, 2004.
- [37] M. Kulmala, T. Vesala, J. Schwarz, J. Smolik, Mass-transfer from a drop .2. theoretical-analysis of temperature-dependent mass flux correlation, *International Journal of Heat and Mass Transfer* 38 (9) (1995) 1705–1708.
- [38] B. Lafaurie, C. Nardone, R. Scardovelli, S. Zaleski, G. Zanetti, Modelling merging and fragmentation in multiphase flows with SURFER, *Journal of Computational Physics* 113 (1) (1994) 134–147.
- [39] G. Lamanna, C. Steinhausen, B. Weigand, A. Preusche, B. Bork, A. Dreizler, R. Stierle, J. Groß, On the importance of non-equilibrium models for describing the coupling of heat and mass transfer at high pressure, *International Communications in Heat and Mass Transfer* 98 (2018) 49 – 58.
- [40] H. Lamb, *Hydrodynamics*, 6th ed., Cambridge University Press, 1932.
- [41] G. Lupo, C. Duwig, A numerical study of ethanol water-droplet evaporation, *Journal of Engineering for Gas Turbines and Power* 140 (2) (2017) 021401–021401–9.
- [42] C. Ma, D. Bothe, Numerical modeling of thermocapillary two-phase flows with evaporation using a two-scalar approach for heat transfer, *Journal of Computational Physics* 233 (2013) 552–573.
- [43] M. Mezhericher, A. Levy, I. Borde, Spray drying modelling based on advanced droplet drying kinetics, *Chemical Engineering and Processing* 48 (11) (2010) 1205–1213.
- [44] A. F. Mills, *Mass Transfer*, Prentice Hall, 2001.
- [45] D. Q. Nguyen, R. P. Fedkiw, M. Kang, A boundary condition capturing method for incompressible flame discontinuities, *J. Comput. Phys* 172 (2001) 71–98.
- [46] B. E. Poling, J. M. Prausnitz, J. P. O’Connell, *The Properties of Gases and Liquids*, fifth edition ed., McGraw-Hill, 2000.
- [47] S. Popinet, An accurate adaptive solver for surface-tension-driven interfacial flows, *Journal of Computational Physics* 228 (16) (2009) 5838–5866.

- [48] S. Popinet, S. Zaleski, A front-tracking algorithm for accurate representation of surface tension, *International Journal For Numerical Methods In Fluids* 30 (6) (1999) 775–793.
- [49] H. R. Pruppacher, J. D. Klett, *Microphysics of clouds and precipitation*, Kluwer Academic Publishers, 1997.
- [50] W. E. Ranz, W. R. Marshall, Evaporation from drops: Part 2, *Chemical Engineering Progress* 48 (4) (1952) 173–180.
- [51] P. Rauschenberger, K. Eisenschmidt, B. Weigand, Volume of fluid based direct numerical simulation of ice growth, in: *83rd Annual Meeting of the International Association of Applied Mathematics and Mechanics*, 2012.
- [52] P. Rauschenberger, B. Weigand, A Volume-of-Fluid method with interface reconstruction for ice growth in supercooled water, *Journal of Computational Physics* 282 (2015) 98–112.
- [53] M. Reitzle, C. Kieffer-Roth, H. Garcke, B. Weigand, A volume-of-fluid method for three-dimensional hexagonal solidification processes, *Journal of Computational Physics* 339 (2017) 356–369.
- [54] M. Reitzle, S. Ruberto, R. Stierle, J. Gross, T. Janzen, B. Weigand, Direct numerical simulation of sublimating ice particles, *International Journal of Thermal Sciences* 145.
- [55] M. Renksizbulut, M. Bussmann, Multicomponent droplet evaporation at intermediate reynolds-numbers, *International Journal of Heat and Mass Transfer* 36 (11) (1993) 2827–2835.
- [56] M. Renksizbulut, R. J. Haywood, Transient droplet evaporation with variable properties and internal circulation at intermediate reynolds-numbers, *International Journal of Multiphase Flow* 14 (2) (1988) 189–202.
- [57] M. Renksizbulut, M. C. Yuen, Numerical study of droplet evaporation in a high-temperature stream, *Journal of Heat Transfer-transactions of the Asme* 105 (2) (1983) 389–397.
- [58] J. Reuttsch, M. Ertl, M. Baggio, A. Seck, B. Weigand, Towards a Direct Numerical Simulation of Primary Jet Breakup with Evaporation, chap. 15, Springer International Publishing, 2019, pp. 243–257.
- [59] J. Reuttsch, G. V. R. Kochanattu, M. Ibach, C. Kieffer-Roth, S. Tonini, G. Cossali, B. Weigand, Direct numerical simulations of oscillating liquid droplets: a method to extract shape characteristics, in: *Proceedings ILASS-Europe 2019. 29th Conference on Liquid Atomization and Spray Systems*, 2019.
- [60] W. J. Rider, D. B. Kothe, Reconstructing volume tracking, *Journal of Computational Physics* 141 (2) (1998) 112–152.

- [61] M. Rieber, Numerical modelling of the dynamic of boundary layers in two phase flows (english translation), Dissertation, Universität Stuttgart (2004).
- [62] M. Rieber, F. Graf, M. Hase, N. Roth, B. Weigand, Numerical simulation of moving spherical and strongly deformed droplets, Proceedings ILASS-Europe (2000) 1–6.
- [63] P. Roache, Verification and Validation in Computational Science and Engineering, Hermosa Publishers, 1998.
- [64] J. Roth, N. and. Schlottke, J. Urban, B. Weigand, Simulations of droplet impact on cold wall without wetting, ILASS (2008) 1–7.
- [65] S. Ruberto, J. Reuttsch, N. Roth, B. Weigand, A systematic experimental study on the evaporation rate of supercooled water droplets at subzero temperatures and varying relative humidity, Experiments in Fluids 58 (5) (2017) 55.
- [66] S. Ruberto, J. Reuttsch, B. Weigand, Experimental investigation of the evaporation rate of supercooled water droplets at constant temperature and varying relative humidity, International Communications in Heat and Mass Transfer 77 (2016) 190 – 194.
- [67] S. S. Sazhin, Advanced models of fuel droplet heating and evaporation, Progress In Energy and Combustion Science 32 (2) (2006) 162–214.
- [68] J. Schlottke, Direct numerical simulation of multiphase flows with phase change (english translation), Ph.D. thesis, Universität Stuttgart (2010).
- [69] J. Schlottke, E. Dülger, B. Weigand, A vof-based 3d numerical investigation of evaporating, deformed droplets, Progress In Computational Fluid Dynamics 9 (6/7) (2009) 426–435.
- [70] J. Schlottke, P. Rauschenberger, B. Weigand, C. Ma, D. Bothe, Volume of Fluid Direct Numerical Simulation of Heat and Mass Transfer using Sharp Temperature and Concentration Fields, in: ILASS - Europe 2011, 24th European Conference on Liquid Atomization and Spray Systems, Estoril, Portugal, 2011.
- [71] J. Schlottke, B. Weigand, Direct numerical simulation of evaporating droplets, Journal of Computational Physics 227 (10) (2008) 5215–5237.
- [72] J. Schwarz, J. Smolik, Mass-transfer from a drop .1. experimental-study and comparison with existing correlations, International Journal of Heat and Mass Transfer 37 (14) (1994) 2139–2143.
- [73] W. Shyy, R. W. Smith, H. S. Udaykumar, M. M. Rao, Computational Fluid Dynamics with Moving Boundaries, CRC Press, Bristol, PA, USA, 1995.


- [74] W. A. Sirignano, Fuel droplet vaporization and spray combustion theory, *Progress in Energy and Combustion Science* 9 (4) (1983) 291–322.
- [75] G. Son, A level-set method for analysis of microdroplet evaporation on a heated surface, *Journal of Mechanical Science and Technology* 24 (4) (2010) 991–997.
- [76] G. Son, Numerical analysis of microdroplet impact and evaporation on a solid surface, in: *Journal of Heat Transfer*, vol. 134, 2011.
- [77] G. Son, V. K. Dhir, Numerical simulation of film boiling near critical pressures with a level set method, *Journal of Heat Transfer-transactions of the Asme* 120 (1) (1998) 183–192.
- [78] G. Son, V. K. Dhir, A level set method for analysis of film boiling on an immersed solid surface, *Numerical Heat Transfer, Part B: Fundamentals* 52 (2) (2007) 153–177.
- [79] G. Son, V. K. Dhir, N. Ramanujapu, Dynamics and heat transfer associated with a single bubble during nucleate boiling on a horizontal surface, *Journal of Heat Transfer-transactions of the Asme* 121 (3) (1999) 623–631.
- [80] G. Son, N. Ramanujapu, V. K. Dhir, Numerical simulation of bubble merger process on a single nucleation site during pool nucleate boiling, *Journal of Heat Transfer* 124 (1) (2001) 51–62.
- [81] C. Steinhausen, J. Reuttsch, G. Lamanna, B. Weigand, R. Stierle, J. Gross, A. Preusche, A. Dreizler, Droplet evaporation under high pressure and temperature conditions: A comparison of experimental estimations and direct numerical simulations, in: *Proceedings ILASS–Europe 2019. 29th Conference on Liquid Atomization and Spray Systems*, 2019.
- [82] G. Strang, On the Construction and Comparison of Difference Schemes, *SIAM Journal on Numerical Analysis* 5 (3) (1968) 506–517.
- [83] M. Sussman, E. G. Puckett, A coupled level set and volume-of-fluid method for computing 3d and axisymmetric incompressible two-phase flows, *Journal of Computational Physics* 162 (2) (2000) 301–337.
- [84] S. Tanguy, T. Menard, A. Berlemont, A level set method for vaporizing two-phase flows, *Journal of Computational Physics* 221 (2) (2007) 837–853.
- [85] S. Tonini, G. Cossali, An exact solution of the mass transport equations for spheroidal evaporating drops, *International Journal of Heat and Mass Transfer* 60 (2013) 236 – 240.
- [86] S. Tonini, G. Cossali, An evaporation model for oscillating spheroidal drops, *International Communications in Heat and Mass Transfer* 51 (2014) 18 – 24.

- [87] S. Tonini, G. Cossali, One-dimensional analytical approach to modelling evaporation and heating of deformed drops, *International Journal of Heat and Mass Transfer* 97 (2016) 301 – 307.
- [88] A.-K. Tornberg, Interface tracking methods with application to multiphase flows, Ph.D. thesis, Tekniska Högskolan, Kungl (01 2000).
- [89] G. Tryggvason, B. Bunner, A. Esmaeeli, D. Juric, N. Al-Rawahi, W. Tauber, J. Han, S. Nas, Y. J. Jan, A front-tracking method for the computations of multiphase flow, *Journal of Computational Physics* 169 (2) (2001) 708–759.
- [90] G. Tryggvason, J. Lu, Direct numerical simulations of flows with phase change, *Procedia IUTAM* 15 (2015) 2 – 13, iUTAM Symposium on Multiphase Flows with Phase Change: Challenges and Opportunities.
- [91] S. O. Unverdi, G. Tryggvason, A front-tracking method for viscous, incompressible, multi-fluid flows, *Journal of Computational Physics* 100 (1) (1992) 25–37.
- [92] B. van Leer, Towards the ultimate conservative difference scheme. v. A second-order sequel to Godunov’s method, *Journal of Computational Physics* 32 (1) (1979) 101–136.
- [93] A. Vogel, S. Reiter, M. Rupp, A. Nägel, G. Wittum, UG4: A novel flexible software system for simulating PDE based models on high performance computers, *Computing and visualization in science* 16 (4) (2013) 165–179.
- [94] W. Wagner, New vapour pressure measurements for argon and nitrogen and a new method for establishing rational vapour pressure equations, *Cryogenics* 13 (8) (1973) 470 – 482.
- [95] S. W. J. Welch, J. Wilson, A volume of fluid based method for fluid flows with phase change, *Journal of Computational Physics* 160 (2) (2000) 662–682.
- [96] H. W. Xiang, L. C. Tan, A new vapor-pressure equation, *International Journal of Thermophysics* 15 (4) (1994) 711–727.
- [97] J.-R. Yang, S.-C. Wong, On the discrepancies between theoretical and experimental results for microgravity droplet evaporation, *International Journal of Heat and Mass Transfer* 44 (23) (2001) 4433–4443.
- [98] J. Young, The condensation and evaporation of liquid droplets at arbitrary knudsen number in the presence of an inert gas, *International Journal of Heat and Mass Transfer* 36 (11) (1993) 2941 – 2956.

Declaration of interests

☒ The authors declare that they have no known competing financial interests or personal relationships that could have appeared to influence the work reported in this paper.

☐ The authors declare the following financial interests/personal relationships which may be considered as potential competing interests:



Geffen Roth

B. Wey